ACS OMEGA

http://pubs.acs.org/journal/acsodf Review

State-of-the-Art β-Ga_2O_3 Field-Effect Transistors for Power Electronics

An-Chen Liu,[#] Chi-Hsiang Hsieh,[#] Catherine Langpoklakpam, Konthoujam James Singh, Wen-Chung Lee, Yi-Kai Hsiao, Ray-Hua Horng,* Hao-Chung Kuo,* and Chang-Ching Tu*

Cite This: *ACS Omega* 2022, 7, 36070−36091

Read Online

ACCESS | Metrics & More | Article Recommendations

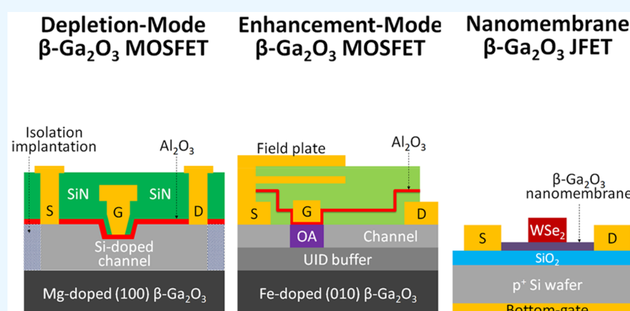

ABSTRACT: Due to the emergence of electric vehicles, power electronics have become the new focal point of research. Compared to commercialized semiconductors, such as Si, GaN, and SiC, power devices based on β-Ga_2O_3 are capable of handling high voltages in smaller dimensions and with higher efficiencies, because of the ultrawide bandgap (4.9 eV) and large breakdown electric field (8 MV cm^{-1}). Furthermore, the β-Ga_2O_3 bulk crystals can be synthesized by the relatively low-cost melt growth methods, making the single-crystal substrates and epitaxial layers readily accessible for fabricating high-performance power devices. In this article, we first provide a comprehensive review on the material properties, crystal growth, and deposition methods of β-Ga_2O_3, and then focus on the state-of-the-art depletion mode, enhancement mode, and nanomembrane field-effect transistors (FETs) based on β-Ga_2O_3 for high-power switching and high-frequency amplification applications. In the meantime, device-level approaches to cope with the two main issues of β-Ga_2O_3, namely, the lack of p-type doping and the relatively low thermal conductivity, will be discussed and compared.

INTRODUCTION

Gallium oxide, as a type of semiconducting sesquioxide, has been known for decades.[1−3] In recent years, owing to the tremendous progress in crystal growth and epitaxy techniques,[4−8] gallium oxide, particularly β-Ga_2O_3, has attracted renewed attention as one of the fourth-generation ultra-wide-bandgap (UWBG) semiconductors, in addition to AlGaN, diamond, and cubic boron nitride.[9] In comparison to the well-established SiC and GaN technologies, β-Ga_2O_3 with a larger energy bandgap (4.9 eV) exhibits higher breakdown electric field (8 MV cm^{-1}) and better Baliga's figure of merit (BFOM) (Table 1), suggesting much less power loss incurred in the power devices based on β-Ga_2O_3.[10−14] The first single-crystal field-effect transistors (FETs) based on β-Ga_2O_3 homoepitaxial layers were demonstrated in 2012.[15] Furthermore, since the β-Ga_2O_3 crystals can be synthesized by various melt growth methods at atmospheric pressure, such as the floating zone (FZ), Czochralski (CZ), and edge-defined film-fed growth (EFG) methods, the cost for producing large-area, uniform, single-crystal substrates can be greatly reduced.[4−6] In contrast, the bulk crystals of SiC and GaN can only be manufactured by the less efficient vapor growth methods, such as the sublimation method for SiC crystals and the sodium flux and ammonothermal methods for GaN crystals.[16−18] So far, β-Ga_2O_3 wafers with diameters up to 4 in. have already been demonstrated or commercialized by companies, such as Tamura, Koha, and Novel Crystal Technology.[6] Due to its UWBG nature, β-Ga_2O_3 has found various optoelectronic applications, including solar-blind deep ultraviolet (DUV) photodetectors and transparent conductive oxide (TCO) electrodes for the light emitting diodes (LEDs).[19,20] Furthermore, the β-Ga_2O_3 nanowires and thin films with extraordinary chemical and thermal stabilities have been explored as highly sensitive gas sensors,[21] and the amorphous and stoichiometric Ga_2O_3 thin films deposited on GaAs (001) substrates can potentially serve as the GaAs gate dielectrics.[22]

As electric vehicles revolutionize the automotive market, power electronics, a vital component of electric powertrains alongside batteries and traction motors, have emerged as a new research focus. The power electronics in electric vehicles mainly include the AC-to-DC rectifiers for charging the batteries, the DC-to-DC converters between high- and low-voltage batteries, and most importantly, the DC-to-AC

Received: May 29, 2022
Accepted: September 16, 2022
Published: October 7, 2022

© 2022 The Authors. Published by American Chemical Society

Table 1. Material Properties, BFOMs, JFOMs, and HCAFOMs of Different Semiconductors, Including Si, GaAs, 4H-SiC, GaN, β-Ga_2O_3, and Diamond[10−14a]

Crystal Type	Crystal Structure	Energy Bandgap (eV)	Dielectric Constant (ϵ_r)	RT Electron Mobility (μ, $cm^2 V^{-1} s^{-1}$)	Breakdown Electric Field (E_{BR}, $MV cm^{-1}$)	Electron Saturation Velocity (v_{sat}, $\times 10^7$ $cm s^{-1}$)	Thermal Conductivity ($W m^{-1} K^{-1}$)	BFOM ($\epsilon_r \mu E_{BR}^3$)	JFOM ($E_{BR} V_{sat}$)	HCAFOM ($\epsilon_r \cdot \mu^{1/2} \cdot E_{BR}^2$)
Si	Face-Centered Cubic	1.1	11.8	1400	0.3	1	150	1	1	1
GaAs	Zinc Blende	1.4	12.9	8000	0.4	1.2	55	15	2	5
4H-SiC	Cubic and Hexagonal	3.3	9.7	1000	2.5	2	270	340	17	48
GaN	Wurtzite	3.4	9.0	1200	3.3	2.5	210	870	28	85
β-Ga_2O_3	Monoclinic	4.9	10	300 (estimated)	8	2	13 [100] 21 [010]	3444	53	279
Diamond	Face-Centered Cubic	5.5	5.5	2000	10	1	1000	24644	33	619

[a]The BFOM, JFOM, and HCAFOM of Si are normalized to 1.

inverters for powering the traction motors. Any performance enhancement in the power devices, particularly high-power inverters, can considerably extend the vehicle driving range with the same battery capacity. Nowadays, the vast majority of electronic systems are built upon Si, and thanks to the modern semiconductor manufacturing technologies, the performance of Si-based devices has improved dramatically over the past few decades. On the other hand, for the power electronics, it was demonstrated that with the same breakdown voltage and device structure, the on-resistance of power transistors is inversely proportional to the third power of the energy bandgap and inversely proportional to the charge carrier mobility.[23] In this regard, the UWBG of β-Ga_2O_3 (4.9 eV) clearly outperforms Si (1.1 eV) and other wide bandgap semiconductors, such as SiC (3.3 eV) and GaN (3.4 eV). Moreover, the high breakdown electric field of β-Ga_2O_3 (8 MV cm^{-1}) allows for much miniaturized device structures, resulting in significant reduction of parasitic capacitance and thus improvement in frequency response. This article aims to provide a comprehensive overview on the material properties, crystal growth and deposition methods of β-Ga_2O_3, and most importantly, the state-of-the-art depletion mode, enhancement mode, and nanomembrane FETs based on β-Ga_2O_3 for high-power switching and high-frequency amplification applications. In the meantime, device-level approaches to cope with the two main issues of β-Ga_2O_3, namely, the lack of p-type doping and the relatively low thermal conductivity compared to SiC and GaN, will be discussed and compared.

■ MATERIAL PROPERTIES OF GALLIUM OXIDE

As early as 1952, various polymorphs of Ga_2O_3 and phase equilibria of the Al_2O_3−Ga_2O_3−H_2O systems were determined.[1] The five polymorphs are α, β, γ, δ, and ε, where the α-phase is corundum, β-phase monoclinic, γ-phase defective spinel, ε-phase orthorhombic, and δ-phase most likely orthorhombic.[1,2,24] In general, the theoretical formation energies of the five polymorphs follow the tendency of $\beta < \varepsilon < \alpha < \delta < \gamma$.[25] As a result, the monoclinic β-Ga_2O_3 is the most stable structure, while the remaining polymorphs are metastable. Furthermore, due to its high melting point of ~1793 °C, β-Ga_2O_3 is the only polymorph whose bulk crystal can be grown by using the melt growth methods.[26] In comparison, the metastable ε-Ga_2O_3 and α-Ga_2O_3 can only withstand temperatures up to 870 and 600 °C, respectively. In fact, all phases of Ga_2O_3 can transition to other phases by annealing and would eventually end up transforming to the most stable β-phase.[1] Therefore, until now the great majority of research on gallium oxide has been devoted to β-Ga_2O_3. On the other hand, the heteroepitaxy of α-Ga_2O_3 and ε-Ga_2O_3 on sapphire substrates has also attracted much attention, because compared to the monoclinic β-Ga_2O_3, the corundum α-Ga_2O_3 and the orthorhombic ε-Ga_2O_3 have a better symmetry match with the hexagonal *c*-plane sapphire substrates.[27−30]

The β-Ga_2O_3 has a monoclinic crystal structure with the space group of $C2/m$ and the lattice constants of a = 12.2 Å, b = 3.0 Å, c = 5.8 Å, and β = 104° (Figure 1).[24] The β-Ga_2O_3 crystal is composed of sixfold coordinated Ga−O octahedra and fourfold coordinated Ga−O tetrahedra. The different arrangements of Ga and O atoms along different directions lead to anisotropic physical properties. For example, the thermal conductivity along the [010] direction is 21 W m^{-1} K^{-1}, while it is 13 W m^{-1} K^{-1} along the [100] direction.[31−33] The static dielectric constants of β-Ga_2O_3 perpendicular to the (100), (010), and (001) planes are also slightly different from each other.[34] The β-Ga_2O_3 crystal structure has two cleavage planes, namely, (100) and (001), and since the lattice parameter along the [100] direction is higher than the [010] and [001] directions, it is easy to exfoliate ultrathin films along the (100) plane direction.[14] After washing with organic solvents and annealing in oxygen ambient, the typical β-Ga_2O_3 wafer surface should exhibit a regular step-and-terrace morphology.[7] The terrace width is a function of the substrate disorientation; the smaller the miscut angle, the larger the

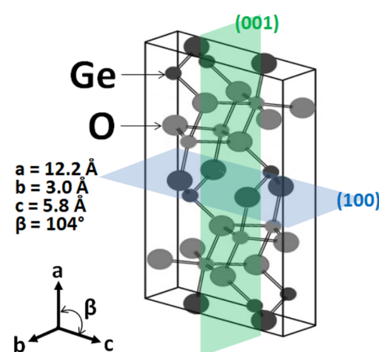

Figure 1. Crystal structure and lattice parameters of β-Ga_2O_3.[24]

https://doi.org/10.1021/acsomega.2c03345
ACS Omega 2022, 7, 36070−36091

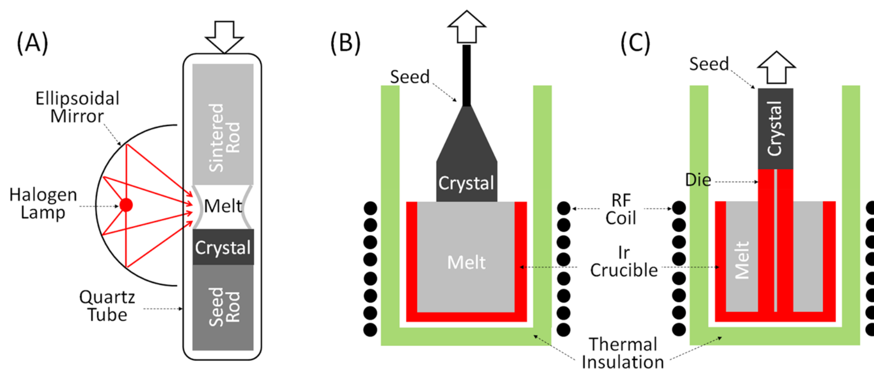

Figure 2. Schematic drawings of (A) the FZ method,[59] (B) the CZ method,[60] and (C) the EFG method,[57] respectively.

terrace width of the substrate. The typical atomic force microscopy (AFM) image reveals that the (100) plane of a β-Ga_2O_3 substrate with a miscut angle of ~0.2° has the terrace width of 70 to 100 nm.[7] During homoepitaxy, the adhesion energy on the terraces of the (100) plane is weaker than at the steps and kinks, therefore promoting the step-flow growth.[35]

The energy bandgap of pure β-Ga_2O_3 has been determined to be 4.7−4.9 eV.[4,36] Therefore, β-Ga_2O_3 should be transparent from the UV to visible range, as evidenced by the crystal clear, 2-in.-diameter Ga_2O_3 wafer synthesized by the EFG method.[37,38] The intrinsic electron mobility in the drift layers of β-Ga_2O_3 power devices is estimated to be 100−300 $cm^2\ V^{-1}\ s^{-1}$ for the electron density 10^{15}−10^{16} cm^{-3}.[15,39] Based on the first-principle band structure calculation, the monoclinic β-Ga_2O_3 has an indirect bandgap of 4.84 eV and a direct bandgap of 4.88 eV, and a relatively light electron effective mass of ~$0.28m_0$, where m_0 is the free electron mass.[40] In contrast, the hole effective mass is very large, because the valence band is relatively flat in the momentum space.[40,41] Therefore, the unintentionally doped (UID) β-Ga_2O_3 is typically n-type with the carrier concentrations in low 10^{17} cm^{-3}. The n-type conductivity can be further enhanced by intentionally doping with the shallow dopants, such as Si, Ge, and Sn. On the contrary, Mg and Fe are often used as the compensating acceptors for obtaining semi-insulating β-Ga_2O_3. For evaluating different semiconductors for the power device application, in addition to the BFOM, which only accounts for the DC conduction loss, the Johnson figure of merit (JFOM, power-frequency product) and the Huang's chip area manufacturing figure of merit (HCAFOM, manufacturability and expense) are also commonly considered. Thanks to the high breakdown electric field (8 MV cm^{-1}), the JFOM and HCAFOM of β-Ga_2O_3 obviously stand out in comparison to Si, GaAs, SiC, and GaN (Table 1).

CRYSTAL GROWTH OF GALLIUM OXIDE

Being able to grow bulk single crystals by using the relatively low-cost melt growth methods is one significant advantage of β-Ga_2O_3. In 1964, the first melt-grown β-Ga_2O_3 crystals were obtained with the use of the Verneuil method.[42] However, not so many relevant research activities had been reported in the following years until 1996, when the FZ method was used to grow β-$Ga_{2-x}In_xO_3$.[43] Later, β-Ga_2O_3 single-crystal boules with diameters up to 8 mm were successfully synthesized by the FZ method.[4,44−48] The starting material of the FZ method is 5N-grade β-Ga_2O_3 powder, which is pressed into rods by a cold isostatic press process (50 to 300 MPa). Then, the rods are sintered at ~1500 °C in air for 10 h. During the crystal growth, the sintered rod is positioned on the upper shaft, slowly rotating in an opposite direction to a β-Ga_2O_3 seed crystal positioned on the lower shaft. Four high-power (1.5 kW) halogen lamps and the corresponding ellipsoidal mirrors are used as the heating system. The growth rate is 1 to 20 mm h^{-1} under dry air or synthetic air (21 vol % O_2 + 79 vol % N_2) flow. The crystal growth process is illustrated in Figure 2A. The major concerns of the FZ method are the collapse of the liquid melt which is barely held by the surface tension and the crack formation in the grown crystal due to high thermal gradients.

The feasibility of using the CZ method with Ir crucibles for growing β-Ga_2O_3 single crystals was demonstrated in 2000,[5] and major improvements have been made since 2010.[49−55] The starting material, 5N-grade β-Ga_2O_3 powder, is first placed in the Ir crucible, which is heated by the surrounding radiofrequency (RF) inductor to form the β-Ga_2O_3 melt. A seed crystal is introduced into the melt and then slowly pulled up (1 to 2 mm h^{-1}) while rotating (5 to 10 rpm). The crystal growth process is illustrated in Figure 2B. The β-Ga_2O_3 cylindrical boules with diameters up to 50 mm can be obtained using this method.[53] The major concern of the CZ method is the decomposition of Ga_2O_3 into volatile species, such as Ga, GaO, and Ga_2O, in an oxygen-deficient atmosphere. On the contrary, the Ir crucible and other Ir parts are prone to oxidation in an oxygen-rich atmosphere. It was found that an appropriate growth atmosphere comprising CO_2, Ar, and O_2, along with overpressure, can effectively suppress the decomposition of Ga_2O_3 without harming the Ir crucible.[49] The influence of other parameters on the grown crystal quality, such as furnace design, crucible aspect ratio, crystal-to-crucible diameter ratio, heating and cooling rates, growth and rotation rates, seed preparation, and crystallization ratio, have also been investigated.[56]

The EFG method, featuring high growth speed and precise control of crystal size and shape via the use of a die, has been applied to the growth of β-Ga_2O_3 since 2008.[6] Similar to the FZ and CZ methods, the starting material of the EFG method is 5N-grade β-Ga_2O_3 powder, which is placed in an Ir crucible along with an Ir die in the middle. The heating of the crucible is carried out by using an RF induction coil. Once the melting point is reached, the β-Ga_2O_3 melt moves up through the slit of the Ir die by capillary force, and a β-Ga_2O_3 seed crystal is positioned in contact with the melt on top of the die to initiate the crystal growth process, as illustrated in Figure 2C.[57] The shape of the grown crystal is determined by the shape of the top surface of the die. The growth rate can reach 15 mm h^{-1} under the growth atmosphere comprising 2 vol % O_2 + 98 vol

https://doi.org/10.1021/acsomega.2c03345
ACS Omega 2022, 7, 36070−36091

Table 2. Homoepitaxy of β-Ga_2O_3 Layers on (100) and (010) β-Ga_2O_3 Substrates, by Various Epitaxy Techniques, Including MOCVD, LPCVD, HVPE, and PA-MBE[a]

	Homoepitaxy				
	Epitaxial Layers	Substrates	Conditions	Crystal Characteristics	ref
(A)	β-Ga_2O_3	(100) β-Ga_2O_3	**MOCVD**: TMGa and O_2 or H_2O; 750−850 °C; 5−100 mBar	Nanocrystals of Ga_2O_3 were formed with O_2 as oxidant, while smooth epitaxial layers of Ga_2O_3 were formed with H_2O as oxidant.	7
(B)	Sn-doped β-Ga_2O_3	(100) β-Ga_2O_3	**MOCVD:** TEGa, O_2, and TESn; 850 °C; 5 mBar	RMS surface roughness of ∼0.6 nm was achieved. The maximum electron mobility of 41 $cm^2\ V^{-1}\ s^{-1}$ was obtained with the carrier concentration equal to $1 \times 10^{18}\ cm^{-3}$.	61
(C)	β-Ga_2O_3	(100) β-Ga_2O_3	**MOCVD:** TEGa and O_2; 850 °C; 5 mBar	The Ga_2O_3 layer grown on a substrate with 0.1° miscut angle exhibited high twin lamella (stacking fault) density, while the layer grown with 6° miscut angle exhibited nearly zero twin lamella.	62
(D)	Sn- and Si-doped β-Ga_2O_3	Fe-doped (010) β-Ga_2O_3	**MOCVD:** TEGa, O_2, TEOS, and TESn; 850 °C; 5 mBar	A RMS surface roughness about 0.6 nm was achieved. No dislocations or planar defects were observed. The maximum electron mobility of about 130 $cm^2\ V^{-1}\ s^{-1}$ was obtained with the carrier concentration equal to $1 \times 10^{17}\ cm^{-3}$ regardless of the dopant type.	64
(E)	β-Ga_2O_3	(010) β-Ga_2O_3	**LPCVD:** Ga pellets and O_2; 780−950 °C	A maximum growth rate of 1.3 μm h^{-1} was obtained at 850 °C, while a RMS surface roughness about 7 nm was obtained at 950 °C.	65
(F)	β-Ga_2O_3	Sn-doped (001) β-Ga_2O_3	**HVPE:** GaCl and O_2; 800−1050 °C; 0.5 mBar for GaCl and 2.5 mBar for O_2	A growth rate approximately 5 μm h^{-1} was obtained at 900 °C and above. The thick layers of β-Ga_2O_3 grown at 1000 °C were smoother at the surface and had higher crystalline perfection than those grown at 800 °C.	66
(G)	β-Ga_2O_3	(100) β-Ga_2O_3	**PA-MBE:** evaporated Ga and O_2 plasma; 800 or 900 °C; Ga beam equivalent pressure (BEP) 1.1×10^{-7} or 2.4×10^{-7} Torr	Ga BEP = 1.5×10^{-7} mBar and 800 °C was the optimal growth condition. A RMS surface roughness of ∼0.5 nm was achieved. The grown films were easily cleaved at the (100) and (001) planes. The easy cleavability of (100) planes facilitates the step-flow growth and terrace formation.	35
(H)	β-Ga_2O_3	(001) β-Ga_2O_3	**PA-MBE:** evaporated Ga and O_2 plasma; 700−800 °C; Ga beam equivalent pressure (BEP) 1.7×10^{-8} or 9.5×10^{-8} Torr	The growth rate increased with increasing Ga BEP, reaching a plateau of 56 nm h^{-1}, and then decreased at higher Ga BEP. The growth rate decreased with the substrate temperature increasing from 750 to 800 °C. The growth rate became negative (i.e., etching) when only Ga flux was supplied.	79

[a]Characteristics of the grown crystals are summarized. TMGa represents trimethylgallium, TEGa triethylgallium, TESn tetraethyltin, and TEOS tetraethylorthosilicate.

https://doi.org/10.1021/acsomega.2c03345
ACS Omega 2022, 7, 36070−36091

Table 3. Heteroepitaxy of β-Ga_2O_3, ε-Ga_2O_3, and α-Ga_2O_3 Layers on *c*-Plane and *a*-Plane Sapphire, 6H-SiC, *c*-Plane GaN, and *c*-Plane AlN/SiC Substrates, by Various Epitaxy Techniques, Including MOCVD, PA-MBE, HVPE, and Mist-CVD[a]

Heteroepitaxy					
	Epitaxial Layers	Substrates	Conditions	Crystal Characteristics	ref
(A)	β-Ga_2O_3	*a*- and *c*-plane sapphire	**MOCVD:** TMGa and O_2, 600−800 °C; 66 mBar	The Ga_2O_3 films grown on *c*-plane sapphire substrates were (−201)-oriented, while the Ga_2O_3 films grown on *a*-plane substrates were less oriented and contained α-phase. The film density (5.6 g cm^{-3}) was lower than the theoretical value (6.4 g cm^{-3}), indicating the presence of gallium or oxygen vacancies.	67
(B)	Sn-doped β-Ga_2O_3	*c*-plane sapphire	**MOCVD:** TMGa, H_2O and TESn, 775−850 °C; 5−50 mBar	The Ga_2O_3 films grown on *c*-plane sapphire substrates were (−201)-oriented with the Sn-doping concentration 10^{17}−10^{19} cm^{-3}. The growth condition 850 °C and 50 mBar led to better crystal quality than 800 °C and 5 mBar. Ga vacancy-related defects and carbon-related complexes act as acceptors.	68
(C)	Si-doped β-Ga_2O_3	*c*-plane sapphire	**MOCVD:** TMGa, H_2O and TEOS, 800 °C; 5 and 10 mBar	The Ga_2O_3 films grown on *c*-plane sapphire substrates were (−201)-oriented. The Si-doping concentration in the range 10^{17}−10^{18} cm^{-3} did not degrade the crystal quality.	8
(D)	β-Ga_2O_3	*c*-plane sapphire	**MOCVD:** TMGa and H_2O, 800 °C; 5−50 mBar	A 3-ML-thick layer of α-Ga_2O_3 was observed at the interface between the β-Ga_2O_3 layer and *c*-plane sapphire substrate. The β-Ga_2O_3 layer was composed of rotational domains due to symmetry mismatch between the monoclinic β-Ga_2O_3 and trigonal α-Ga_2O_3.	69
(E)	ε-Ga_2O_3	*c*-plane Sapphire	**MOCVD:** TMGa and H_2O; 550, 650, and 715 °C; 100 mBar	If the growth temperature was 550 °C, the deposited films were amorphous. If the growth temperature was increased to 715 °C, (−201)-oriented β-Ga_2O_3 with poor crystalline quality was obtained. Only when the growth temperature was controlled at 650 °C was high quality ε-Ga_2O_3 obtained.	72
(F)	β-Ga_2O_3 ε-Ga_2O_3	*c*-plane sapphire	**MOCVD:** TEGa and O_2; 450−570 °C; 12.1 mBar	The Ga_2O_3 films grown on the *c*-plane sapphire substrates were polycrystalline. If the growth temperature was above 535 °C, pure (−201)-oriented β-Ga_2O_3 was obtained. If the growth temperature was 505 °C, a mixture of β-Ga_2O_3 and ε-Ga_2O_3 was obtained.	76
(G)	ε-Ga_2O_3	6H-SiC	**MOCVD:** TEGa and O_2; 500 °C; 35 mBar	The Ga_2O_3 films grown on 6H-SiC substrates were ε-phase pure and in high crystal quality. If annealed at 850 °C, transition to (−201)-oriented β-Ga_2O_3 started to occur. If annealed at 900 °C, all ε-Ga_2O_3 was converted to β-Ga_2O_3.	77
(H)	β-Ga_2O_3	*c*-plane sapphire	**PA-MBE:** evaporated Ga and O_2 plasma; 600−750 °C; Ga beam equivalent pressure (BEP) 5×10^{-9} to 2×10^{-7} Torr	The Ga_2O_3 films grown on *c*-plane sapphire substrates were (−201)-oriented and β-phase pure. With the low Ga flux (high growth rate), three-dimensional columnar structures were obtained. With the high Ga flux (low growth rate), a typical terrace surface morphology was obtained.	78
(I)	β-Ga_2O_3	*a*- and *c*-plane sapphire	**PA-MBE:** evaporated Ga and O_2 plasma; 600−800 °C; 5×10^{-4} Torr	The Ga_2O_3 films grown on *c*-plane and *a*-plane substrates were both (−201)-oriented, with no α-phase diffraction peak observed. Six types of β-Ga_2O_3 grains on the *c*-plane substrate, with the orientation rotated every 60° from the Al_2O_3 [110] direction, were observed.	80
(J)	ε-Ga_2O_3	*c*-plane GaN; *c*-plane AlN/SiC	**HVPE:** Ga, HCl and O_2; 550 °C; 2.5 mBar for HCl and 10 mBar for O_2	A growth rate of approximately 20 μm h^{-1} was achieved for ε-Ga_2O_3 on ε-plane AlN/SiC substrates. The as-grown films on GaN and AlN/SiC substrates were (0001)-oriented ε-phase pure. The ε-Ga_2O_3 film was thermally stable up to 700 °C and exhibited an optical bandgap equal to 4.9 eV.	29
(K)	α-Ga_2O_3	*c*-plane sapphire	**Mist-CVD:** Gallium acetylacetonate $Ga(C_5H_8O_3)_3$ in deionized water with slight addition of HCl; 470 °C	The as-grown α-Ga_2O_3 was phase pure and remained so after annealing at 550 °C. However, if the annealing temperature increased to 600 °C, α- to β-phase transition started to occur. The α-phase completely disappeared at 700 °C.	82

[a]Characteristics of the grown crystals are summarized. TMGa represents trimethylgallium; TEGa, triethylgallium; TESn, tetraethyltin; and TEOS, tetraethylorthosilicate.

https://doi.org/10.1021/acsomega.2c03345
ACS Omega 2022, 7, 36070−36091

% N_2. Later, the pulling rate and die geometry of the EFG method were further optimized to improve the grown crystal quality and shape.[58] It is worth mentioning that for the FZ, CZ, and EFG methods discussed above, the doping of the β-Ga_2O_3 crystals is usually accomplished by mixing the dopants, such as SnO_2 and SiO_2, with the starting materials, β-Ga_2O_3 powder, before the crystal growth process.

DEPOSITION OF GALLIUM OXIDE

Homoepitaxy by MOCVD. Among various deposition methods, metal−organic chemical vapor deposition (MOCVD) has drawn much attention, because it is most suitable for large-scale production and has precise control of growth rate and doping. For the homoepitaxy of β-Ga_2O_3 by MOCVD, (100)- and (010)-oriented wafers are generally used. In 2014, Wagner et al. demonstrated homoepitaxy of β-Ga_2O_3 on a (100) substrate by using trimethylgallium (TMGa) as the gallium precursor and oxygen gas or water as the oxygen precursor (Table 2A).[7] When using pure oxygen gas, the formation energy of oxygen vacancies is greatly increased, and the byproduct $Ga_2(CO_3)_3$ may act as deposition masks, resulting in Ga_2O_3 nanocrystals instead of coherent films. In contrast, when using water as the oxygen source, since the oxygen part is fully consumed by the reaction with gallium, the formation of carbonate-related byproducts is prevented and the remaining hydrogen part may form Ga−H passivation, which can reduce the surface state density and promote the layer-by-layer growth.[7] In 2016, Baldini et al. demonstrated homoepitaxy of n-type β-Ga_2O_3 on a (100) substrate by using triethylgallium (TEGa), oxygen gas, and tetraethyltin (TESn) as the precursors (Table 2B).[61] Despite the ultraflat surface with the root-mean-square (RMS) surface roughness of only ∼0.6 nm, the transmission electron microscopy (TEM) analysis reveals stacking faults in the form of twin lamellae, which may act as the compensation and scattering centers of electrons, limiting the electron mobility.[61] To resolve this issue, it was found that using substrates with relatively large miscut angles can effectively avoid the formation of twin lamellae (Table 2C).[62] For example, the β-Ga_2O_3 layer homoepitaxially grown on a 0.1° miscut (100) substrate has an estimated twin lamella density as high as 1×10^{17} cm^{-3}. In contrast, if the miscut angle is increased to 6°, β-Ga_2O_3 layers free of twin lamella can be achieved. Considering the relatively low diffusion coefficient of gallium at the gas−solid interface (7×10^{-9} cm^2 s^{-1} at 850 °C), the substrate with a small miscut angle has larger terrace width and therefore a higher chance of forming two-dimensional islands which further lead to the stacking faults.[62] For example, the 0.1° miscut (100) β-Ga_2O_3 substrate exhibits a wide terrace, and the as-grown epitaxial layer has elongated islands on the surface and contains a high density of twin lamellae. In contrast, the 4° miscut substrate yields a narrow terrace, few two-dimensional islands, and sporadic twin lamellae.[62] Finally, quantitative calculations using Read's model of charged dislocations confirm the reduction of electron mobility caused by the twin lamellae.[63]

In general, the β-Ga_2O_3 films grown on the (010) β-Ga_2O_3 substrates have higher crystalline perfection than on the (100) β-Ga_2O_3 substrates. Besides, the maximum electron mobility achieved by the (100) β-Ga_2O_3 films so far is only ∼40 cm^2 V^{-1} s^{-1},[61] while the electron mobility of the (010) β-Ga_2O_3 films grown by molecular-beam epitaxy (MBE) can be >100 cm^2 V^{-1} s^{-1}.[39] Furthermore, the heat transfer along the [010] direction (21 W m^{-1} K^{-1}) is more efficient than along the [100] direction (13 W m^{-1} K^{-1}),[31,32] making the (010) β-Ga_2O_3 films more advantageous for the power device application due to the faster heat dissipation. Therefore, in this paragraph we focus on the homoepitaxial growth of β-Ga_2O_3 on the (010) substrates by MOCVD. In 2017, Baldini et al. demonstrated homoepitaxy of Si- and Sn-doped β-Ga_2O_3 on Fe-doped (010) substrates (Table 2D).[64] The as-grown layers are ultraflat with the RMS surface roughness only ∼0.6 nm and are exempt of dislocations or planar defects. Furthermore, due to the very high crystalline perfection, there is no distinguishable interface between the epitaxial layer and the (010) substrate.[64] Compared to Sn, Si is the better dopant because it has higher doping efficiency and no memory effect. The maximum electron mobility equal to ∼130 cm^2 V^{-1} s^{-1} can be achieved with the carrier concentration equal to 1×10^{17} cm^{-3} regardless of the dopant type.[64]

Homoepitaxy by Other Techniques. In 2016, Rafique et al. demonstrated homoepitaxy of (010) β-Ga_2O_3 films by low pressure CVD (LPCVD) and investigated the influence of growth temperature on the crystal quality (Table 2E).[65] With sufficiently high growth temperatures, the deposited crystals achieve high crystalline perfection, i.e., undifferentiable interface between the epitaxial layer and substrate, and the surface morphology exhibits a terrace-like structure, which basically reproduces the substrate's terrace morphology.[65] The RMS surface roughness is ∼40 nm with the growth temperature equal to 780 °C but only ∼7 nm if the growth temperature increases to 950 °C.[65] In 2015, Murakami et al. demonstrated that thick layers of β-Ga_2O_3 can be homoepitaxially grown on (001)-oriented Sn-doped β-Ga_2O_3 substrates by halide vapor phase epitaxy (HVPE) with gaseous GaCl and O_2 as the precursors, and the influence of growth temperature on the crystal quality was investigated (Table 2F).[66] Compared to those grown at 800 °C, the β-Ga_2O_3 layers grown at 1000 °C are much smoother at the surface and have higher crystalline perfection, as revealed by the narrower X-ray rocking curves. In 2008, Oshima et al. demonstrated homoepitaxy of β-Ga_2O_3 layers on (100) β-Ga_2O_3 substrates by plasma-assisted MBE (PA-MBE) using evaporated Ga and O_2 plasma (Table 2G).[35] The deposited films and the substrate exhibit the same β-Ga_2O_3 (020) X-ray diffraction (XRD) peaks, and the film surface morphology features a duplicate of the substrate terrace with the RMS surface roughness only ∼0.5 nm. The grown films can be easily cleaved at the (100) and (001) planes. The excellent cleavability of the (100) planes facilitates the step-flow growth and terrace formation.[35] In 2018, Oshima et al. studied how the Ga-flux and the substrate temperature affect the PA-MBE growth rate (Table 2H).[79] The growth rate of β-Ga_2O_3 increases with higher Ga-flux, reaching a plateau of 56 nm h^{-1}. Further increase of Ga-flux decreases the growth rate. The growth rate also declines with the substrate temperature elevating from 750 to 800 °C. Noticeably, the growth rate becomes negative, i.e., net etching, when only Ga-flux is supplied.[79]

Heteroepitaxy by MOCVD. For the heteroepitaxy of β-Ga_2O_3 by MOCVD, *c*-plane sapphire substrates are most commonly used. The sapphire substrates are relatively cheap and able to provide electrical isolation for the power FETs. In 2016, Tadjer et al. compared the *a*-plane and *c*-plane sapphire substrates for the heteroepitaxy of β-Ga_2O_3 (Table 3A).[67] Based on the XRD analysis, the β-Ga_2O_3 layer grown on the *c*-plane substrate reveals clear β-phase diffraction peaks attributed to the (−201) plane, while the β-Ga_2O_3 layer

https://doi.org/10.1021/acsomega.2c03345
ACS Omega 2022, 7, 36070−36091

grown on the *a*-plane substrate exhibits an obvious α-phase diffraction peak along with some other β-phase diffraction peaks, suggesting a less crystalline and less oriented crystal structure.[67] Besides, the deposited film density (5.6 g cm^{-3}) is significantly lower than the theoretical value (6.4 g cm^{-3}), indicating the presence of gallium or oxygen vacancies.[67] Another study of heteroepitaxy of Sn-doped β-Ga_2O_3 on *c*-plane sapphire substrates also suggested that the grown films are clearly monoclinic and (−201)-oriented with the Sn doping concentration 10^{17}–10^{19} cm^{-3} (Table 3B).[68] However, the Ga vacancy-related defects and the residual carbon complexes from the TMGa precursors may act as acceptors which compensate the Sn donors.[68] Similarly, the Si-doped β-Ga_2O_3 epitaxial layers on *c*-plane sapphire substrates were also (−201)-oriented, and no deterioration of crystal quality was observed in the doping range 10^{17}–10^{18} cm^{-3} (Table 3C).[8] However, when the Si doping concentration is up to 5×10^{19} cm^{-3}, amorphization of the films occurs and only very low conductivity is obtained.[8] On the other hand, different grains or domains have been observed in the heteroepitaxially grown β-Ga_2O_3. In 2015, Schewski et al. found a 3-ML-thick layer of crystalline α-Ga_2O_3 sandwiched between the β-Ga_2O_3 epitaxial layer and *c*-plane sapphire substrate (Table 3D).[69] Besides, the β-Ga_2O_3 layer on top of the α-Ga_2O_3 layer is composed of rotational domains, which can be attributed to the symmetry mismatch between the monoclinic β-Ga_2O_3 and trigonal α-Ga_2O_3.[69] Furthermore, despite the pure β-phase XRD pattern shown, the TEM investigation reveals that the β-Ga_2O_3 epitaxial layer actually contains in-plane grains rotated 120° to each other.[68] Moreover, the actual lattice constants *a* and *c* are estimated to be smaller and the lattice constant *b* and angle β are estimated to be larger, compared to the standard values of single-crystal β-Ga_2O_3.[70] In summary, while the (−201)-oriented β-Ga_2O_3 can indeed grow on the *c*-plane sapphire substrate epitaxially, the grown films can hardly be single-crystal due to the symmetry mismatch between the monoclinic β-Ga_2O_3 and hexagonal Al_2O_3.

Compared to the monoclinic β-Ga_2O_3, the crystallographic symmetry of orthorhombic ε-Ga_2O_3 is better matched to the sapphire substrates.[71] Besides, the ε-Ga_2O_3 also possesses the wide bandgap nature of the β-Ga_2O_3 and can be grown in a relatively mild condition. In 2016, Boschi et al. found that the growth temperature plays a critical role in deciding the crystal form (Table 3E).[72] For example, the films deposited at 550 °C are basically amorphous. If the growth temperature elevates to 715 °C, only weak and broad XRD peaks related to the (−201)-oriented β-Ga_2O_3 are observed, as the crystalline β-Ga_2O_3 are usually obtained at higher temperatures. However, when the growth temperature is controlled at 650 °C, intense and narrow XRD peaks corresponding to the ε-Ga_2O_3 are shown.[72] Furthermore, although the SEM images showed hexagonal nucleation islands at the film surface and the large-area electron diffraction patterns suggested pseudohexagonal symmetry with the $P6_3mc$ space group,[72] the actual structure of ε-Ga_2O_3 is composed of ordered 120°-rotational twin domains, each of which has diameters of 5 to 10 nm and orthorhombic symmetry with the $Pna2_1$ space group.[73] The high-resolution cross-section TEM image indicates that the ε-Ga_2O_3 film grown at 650 °C possesses a columnar structure and γ-Ga_2O_3 epitaxial islands are present at the interface between the ε-Ga_2O_3 film and *c*-plane sapphire substrate.[73] Based on the photon energy for the onset of photoconductivity and band-to-band absorption, the optical bandgap of the ε-Ga_2O_3 films is between 4.6 and 4.7 eV, which is close to that of β-Ga_2O_3, and the cathodoluminescence spectroscopy indicates a group of deep donors located at ∼0.7 eV below the conduction band and three defect states below the midgap.[74] Lastly, the thermal stability of the ε-Ga_2O_3 films grown on *c*-plane sapphire substrates was investigated via differential scanning calorimetry (DSC), TEM, and XRD (Table 3F).[75,76] After heteroepitaxy at 650 °C, the film was placed inside a tubular furnace for the heat treatment. The film can withstand prolonged heat treatment up to 700 °C. However, if the annealing temperature is higher than 900 °C, a complete transition to the β-phase occurs.[75] Similar thermally induced transition was observed for the ε-Ga_2O_3 films grown on 6H-SiC substrates by MOCVD (Table 3G).[77] The as-grown films are ε-phase pure and in high crystal quality. However, the diffraction peaks corresponding to the (−201)-oriented β-Ga_2O_3 start to appear if the annealing temperature increases to 850 °C, and the ε-Ga_2O_3 is completely converted to β-Ga_2O_3 if annealed at 900 °C.[77]

Heteroepitaxy by Other Techniques. In 2010, Tsai et al. demonstrate that by using PA-MBE, phase pure, (−201)-oriented β-Ga_2O_3 films were successfully deposited on *c*-plane sapphire substrates (Table 3H).[78] With the low gallium flux which leads to high growth rate, the as-grown film is composed of three-dimensional columnar structures. On the contrary, with the high gallium flux and thus low growth rate, a typical terrace surface morphology is obtained.[78] The decreasing growth rate with increasing gallium flux is likely due to the formation and desorption of gallium suboxides and was also observed in another PA-MBE work (Table 2H).[79] In 2012, Nakagomi et al. compared the (−201)-oriented β-Ga_2O_3 films heteroepitaxially grown on *c*-plane and *a*-plane sapphire substrates by PA-MBE (Table 3I).[80] Both types of the sapphire substrates can lead to strong (−201)-oriented β-Ga_2O_3 XRD patterns.[80] In contrast, the β-Ga_2O_3 film grown on the *a*-plane sapphire substrate by MOCVD includes certain α-Ga_2O_3.[67] Moreover, the β-Ga_2O_3 film on the *c*-plane sapphire substrate contains six types of grains, with the orientation rotated every 60° from the Al_2O_3 [110] direction.[80] Similar results have also been observed for other β-Ga_2O_3 films grown by MOCVD.[68,69] In 2015, Oshima et al. demonstrated heteroepitaxy of ε-Ga_2O_3 and β-Ga_2O_3 on various substrates, including sapphire, GaN, and AlN/SiC, by using HVPE (Table 3J).[29,81] Compared to MOCVD, the major advantage of HVPE is the relatively high growth rate (approximately 20 μm h^{-1} for ε-Ga_2O_3 grown on *c*-plane AlN/SiC substrates and 250 μm h^{-1} for β-Ga_2O_3 quasi-epitaxially grown on off-angled *c*-plane sapphire substrates), and the crystal qualities of the as-grown films are comparable to those grown by MOCVD.[29,81] In 2013, Lee et al. demonstrated that mist-CVD can be a low-energy-consumption alternative to grow α-Ga_2O_3 films on *c*-plane sapphire substrates (Table 3K).[27,82] Compared to the monoclinic β-Ga_2O_3, the corundum α-Ga_2O_3 is better matched to the hexagonal sapphire substrates, resulting in epitaxial layers with fewer defects. After growth at 470 °C with optimal flow rates, the α-Ga_2O_3 films were annealed at different temperatures step-by-step. The α-phase can be maintained for the annealing temperature up to 550 °C but gradually converted to β-phase if the annealing temperature higher than 600 °C.[82]

■ DEPLETION-MODE β-GA_2O_3 FETS

Given the difficulty of p-type doping in β-Ga_2O_3, recent device performance milestones have been mainly achieved by the

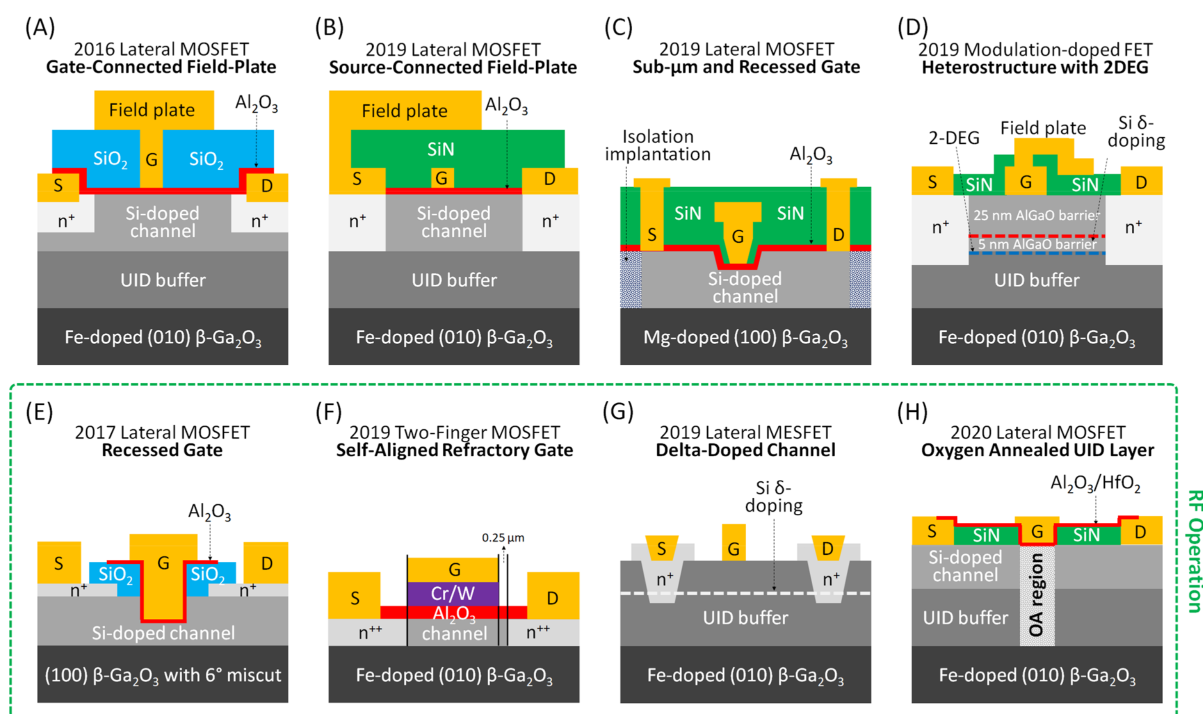

Figure 3. Cross-section illustrations of representative depletion-mode β-Ga_2O_3 FETs, including (A) MOSFET with a gate-connected field-plate,[84] (B) MOSFET with a source-connected field-plate,[92] (C) MOSFET with a sub-μm and recessed gate,[94] (D) heterostructure FET with 2DEG channel,[97] (E) MOSFET with a recessed gate for RF operation,[106] (F) two-finger MOSFET with a self-aligned refractory gate for RF operation,[107] (G) MESFET with a delta-doped channel for RF operation,[108] and (H) MOSFET with an oxygen annealed UID layer for RF operation.[109]

depletion-mode FETs based on epitaxial layers grown on single-crystal β-Ga_2O_3 substrates. For the power switching application, the essential parameter for evaluating the device performance is the power figure of merit (PFOM) = $V_{br}^2/R_{on,sp}$, where V_{br} (V) is the three-terminal off-state breakdown voltage and $R_{on,sp}$ (mΩ cm^2) is the on-resistance normalized by the device area. To exploit the full potential of β-Ga_2O_3 as predicted by the BFOM,[83] many device-level approaches have been developed to increase V_{br} while decreasing $R_{on,sp}$, as discussed below.

Gate-Connected Field-Plates. For metal-oxide-semiconductor FETs (MOSFETs), the gate-connected field-plate is a useful design to manage the electric field distribution between the gate and drain, so that the peak electric field in the channel region will not exceed the breakdown electric field of β-Ga_2O_3 (8 MV cm^{-1}). In 2016, Wong et al. demonstrated depletion-mode β-Ga_2O_3 MOSFETs with gate-connected field-plates for the first time (Figure 3A).[84] An area-selective Si-ion implantation technique was employed to fabricate the channel region and the source/drain (S/D) regions on an UID epitaxial layer grown on a Fe-doped (010) β-Ga_2O_3 substrate by ozone assisted (OA)-MBE. By using Silvaco two-dimensional device simulations, the most favorable field-plate geometry, which balances the peak electric fields among the drain, gate, and field-plate, can be obtained. The β-Ga_2O_3 MOSFET with the optimized field-plate design can achieve V_{br} = 755 V, $R_{on,sp}$ ~ 55 mΩ cm^2, and PFOM ~ 10.4 MW cm^{-2} (Table 4B).[84] In comparison, without the gate-connected field-plate, a similar depletion-mode β-Ga_2O_3 MOSFET can only achieve V_{br} = 370 V, $R_{on,sp}$ ~ 69 mΩ cm^2, and PFOM ~ 2 MW cm^{-2} (Table 4A).[85] Another major difference between the two devices is the incorporation of an UID layer below the channel region.[84] The highly resistive UID buffer layer can protect the channel against charge compensation due to the outdiffusion of Fe deep acceptors from the Fe-doped (010) β-Ga_2O_3 substrate,[86] while providing effective device isolation without the need of mesa etching.[84]

Ge-Doped Channels and Fluorinert Immersion. In 2017, Moser et al. demonstrated two-finger depletion-mode β-Ga_2O_3 MOSFETs with the channel regions doped with Ge (6.1×10^{17} cm^{-3}) and mesa etching for device isolation.[87] Compared to other β-Ga_2O_3 MOSFETs having similar device structures but with the channel regions doped with Sn (1.7×10^{18} cm^{-3}),[88] the two devices can achieve comparable PFOMs of ~11 MW cm^{-2}, but the device with Ge doping exhibits significantly higher channel electron mobility (111 cm^2 V^{-1} s^{-1}) than the device with Sn doping (19.7 cm^2 V^{-1} s^{-1}) (Table 4C and D), suggesting Ge might be a better dopant kind than the commonly used Si or Sn. In 2018, Zheng et al. demonstrated depletion-mode β-Ga_2O_3 MOSFETs with not only gate-connected field-plates but also Fluorinert FC-770 immersion.[89] It was reported that the breakdown through air, which has the dielectric strength of ~3 kV mm^{-1}, might be the major premature breakdown mechanism limiting the V_{br} within 300−400 V.[90,91] Therefore, by replacing air with Fluorinert FC-770, which has the dielectric strength higher than 15 kV mm^{-1}, the V_{br} of the gate field-plated MOSFET can be significantly improved from 440 V in air to 1850 V in Fluorinert. However, due to the relatively long channel length (28 μm), the $R_{on,sp}$ of the device is ~2000 mΩ cm^2, resulting in relatively low PFOM of ~1.7 MW cm^{-2} (Table 4F).[89]

Source-Connected Field-Plates. In 2019, Lv et al. demonstrated depletion-mode β-Ga_2O_3 MOSFETs with source-connected field-plates as an improvement to gate-connected field-plates (Figure 3B).[92] The Si-doped channel layer and the UID buffer layer were homoepitaxially grown on

https://doi.org/10.1021/acsomega.2c03345
ACS Omega 2022, 7, 36070−36091

Table 4. Representative Depletion-Mode β-Ga_2O_3 FETs with Various Device Structures and Fabricated by Different Deposition Techniques[a]

Depletion-Mode β-Ga_2O_3 FETs										
	Features	Substrates/Gates Dielectric	Epitaxial Layers	Donor Concentrations	V_{br} (V)	$R_{on,sp}$ (mΩ cm^2)	$V_{br}^2/R_{on,sp}$ (MW cm^{-2})	$I_{ds,sat}$ (mA mm^{-1})	I_{on}/I_{off}	ref
(A)	• Circular MOSFET • Annealed Ti/Au for ohmic contacts • Si implantation for S/D	Fe-doped (010) β-Ga_2O_3/ 20 nm Al_2O_3	• MBE • 0.30 μm Sn-doped channel	• Channel: Sn, 7×10^{17} cm^{-3} • S/D: Si, 5×10^{19} cm^{-3}	370 ($V_{GS} = -20$ V)	~69 ($V_{GS} = 4$ V)	~2.0	39 ($V_{GS} = 4$ V)	$>10^{10}$	2013[85]
(B)	• Lateral MOSFET • Gatefield-plate • Si implantation for channel and S/D • UID layer for device isolation	Fe-doped (010) β-Ga_2O_3/ 20 nm Al_2O_3	• OA-MBE • 0.30 μm Si-doped channel • 0.90 μm UID buffer layer	• Channel: Si, 3×10^{17} cm^{-3} • S/D: Si, 5×10^{19} cm^{-3}	755 ($V_{GS} = -55$ V)	~55 ($V_{GS} = 4$ V)	~10.4	78 ($V_{GS} = 4$ V)	$>10^{9}$	2016[84]
(C)	• Two-finger MOSFET • Channel $\mu_n = 19.7$ cm^2 V^{-1} s^{-1} (by Hall effect) • Mesa etching for device isolation	Mg-doped (100) β-Ga_2O_3/ 20 nm Al_2O_3	• MOCVD • 0.20 μm Sn-doped channel	• Channel: Sn, 1.7×10^{18} cm^{-3}	230 (V_{GD}) ($V_{GS} = -30$ V)	4.9 ($V_{GS} = 0$ V)	11	~60 ($V_{GS} = 0$ V)	~10^{7}	2016[88]
(D)	• Two-finger MOSFET • Channel $\mu_n = 111$ cm^2 V^{-1} s^{-1} (by Hall effect) • Mesa etching for device isolation	Fe-doped (010) β-Ga_2O_3/ 20 nm Al_2O_3	• MBE • 0.20 μm Ge-doped channel	• Channel: Ge, 6.1×10^{17} cm^{-3}	479 ($V_{GS} = -20$ V)	~20 ($V_{GS} = 0$ V)	~11.5	80 ($V_{GS} = 0$ V)	$>10^{8}$	2017[87]
(E)	• Lateral MOSFET • SOG doping for S/D • Specific contact resistance = 2.1×10^{-5} Ω cm^{-2} • UID layer for device isolation	Fe-doped (010) β-Ga_2O_3/ 20 nm SiO_2	• OA-MBE • 0.20 μm Sn-doped channel • 0.20 μm UID buffer layer	• Channel: Sn, 1×10^{18} cm^{-3} • S/D: Sn, $>10^{21}$ cm^{-3} by SOG	382 ($V_{GS} = -25$ V)	~171 ($V_{GS} = 14$ V)	~0.9	35 ($V_{GS} = 14$ V)	~10^{8}	2017[103]
(F)	• Lateral MOSFET • Gate field-plate • SOG doping for S/D • Fluorinert Immersion • UID layer for device isolation	Fe-doped (010) β-Ga_2O_3/ 20 nm SiO_2	• MBE • 0.20 μm Sn-doped channel • 0.20 μm UID buffer layer	• Channel: Sn, 2×10^{17} cm^{-3} • S/D: Sn, $>10^{21}$ cm^{-3} by SOG	• 1850 in Fluorinert • 440 in air ($V_{GS} = -32$ V)	~2000 in Fluorinert ($V_{GS} = 12$ V)	~1.7	1.5 ($V_{GS} = 12$ V)	~10^{8}	2018[89]
(G)	• Lateral MOSFET • Source field-plate • Si implantation for S/D • SiN_x internal passivation • Mesa etching for device isolation	Fe-doped (010) β-Ga_2O_3/ 25 nm Al_2O_3	• MOCVD • 0.24 μm Si-doped channel • 0.40 pm UID buffer layer	• Channel: Si, 8×10^{17} cm^{-3} • S/D: Si, ~10^{20} cm^{-3}	• 480 with $L_{SD} = 11$ μm • 680 with $L_{SD} = 18$ μm ($V_{GS} = -55$ V)	• 4.58 with $L_{SD} = 11$ μm • 11.7 with $L_{SD} = 18$ μm ($V_{GS} = 5$ V)	• 50.4 with $L_{SD} = 11$ μm • 39.5 with $L_{SD} = 18$ μm	• 267 with $L_{SD} = 11$ μm • 222 with $L_{SD} = 18$ μm ($V_{GS} = 5$ V)	~10^{6}	2019[92]
(H)	• Lateral MOSFET • Source field-plate	Fe-doped (010) β-Ga_2O_3/ 20 nm Al_2O_3	• OA-MBE • 0.15 μm Si-doped channel	• Channel: Sn, 1.5×10^{18} cm^{-3}	2321 in Fluorinert ($V_{GS} = -10$ V)	959 ($V_{GS} = 1$ V)	5.6	~6.5 ($V_{GS} = 1$ V)	~10^{7}	2019[93]

https://doi.org/10.1021/acsomega.2c03345
ACS Omega 2022, 7, 36070−36091

Table 4. continued

	Depletion-Mode β-Ga_2O_3 FETs								
	Features	Substrates/Gates Dielectric	Epitaxial Layers	Donor Concentrations	V_{br} (V)	$R_{on,sp}$ (mΩ cm^2)	$V_{br}^2/R_{on,sp}$ (MW cm^{-2})	$I_{ds,sat}$ (mA mm^{-1})	I_{on}/I_{off}	ref
	• Thin and heavily doped channel • Mesa etching for device isolation									
(I)	• Lateral MOSFET • 0.7-μm-long and recessed gate • SiN_x internal passivation • Multiple energy nitrogen implantation for device isolation	Mg-doped (100) β-Ga_2O_3 with 6° miscut/25 nm Al_2O_3	• MOCVD • 0.20 μm Si-doped channel	• Channel: 2.3 × 10^{17} cm^{-3} (charge carrier)	1830 (V_{GS} = −20 V) (L_{GD} = 10 μm)	21.6 (V_{GS} = 10 V) (L_{GD} = 10 μm)	155	120 (V_{GS} = 10 V)	>10^{10}	2019[94]
(J)	• Lateral MOSFET • CF_4 plasma treatment for n-type doping • β-Ga_2O_3 epitaxial layer on sapphire substrate	*c*-plane Sapphire/40 nm Al_2O_3	• HVPE • 0.15 μm Si-doped channel	• Channel: F, 2.3 × 10^{18} cm^{-3} at 5−10 nm deep from the surface	~155 (V_{GS} < −21 V)	~47k (V_{GS} = −12 V)	~5 × 10^{-4}	~1 × 10^{-1}	~10^6	2021[99]
(K)	• Modulation-doped heterostructured FET • Gate field-plate • Patterned regrowth of n^+ β-Ga_2O_3 for S/D • SiN_x internal passivation • Mesa etching for device isolation	Fe-doped (010) β-Ga_2O_3/Pt/Au Schottky gate contact	• PA-MBE • β-$(Al_{0.22}Ga_{0.78})_2O_3$ 5 nm spacer and 25 nm barrier • 0.10 μm UID buffer layer	• Channel (2DEG): 1.85 × 10^{12} cm^{-2} • S/D: Si, ~10^{20} cm^{-3}	1365 (V_{GS} = −5 V) (L_{SD} = 16 μm)	120.1 (V_{GS} = 0 V) (L_{GD} = 16 μm)	15.5	41 (V_{GS} = 2 V)	~10^7	2019[97]

[a]For each power device, the parameters for evaluating the power switching performance are summarized, including the three-terminal off-state breakdown voltage (V_{br}), on-resistance normalized by the device area ($R_{on,sp}$), power figure of merit (PFOM = $V_{br}^2/R_{on,sp}$), maximum saturation drain current ($I_{ds,sat}$) and I_{on}/I_{off} ratio.

https://doi.org/10.1021/acsomega.2c03345
ACS Omega 2022, 7, 36070−36091

a Fe-doped (010) β-Ga_2O_3 substrate by MOCVD, and then the S/D regions were formed by area-selective Si-ion implantation. The MOSFET with the optimized field-plate design and the channel length (L_{SD}) = 11 μm can achieve V_{br} = 480 V, $R_{on,sp}$ = 4.58 mΩ cm^2, and PFOM = 50.4 MW cm^{-2}. When the L_{SD} was extended to 18 μm, although the V_{br} could increase to 680 V, the $R_{on,sp}$ increased to 11.7 mΩ cm^2 accordingly, making the PFOM slightly decreased to 39.5 MW cm^{-2} (Table 4G).[92] In 2019, Mun et al. further improved the source-connected field-plate design by adopting a thin and heavily doped channel. Besides, the deposition conditions for the Al_2O_3 gate dielectric and SiO_2 internal passivation were optimized, leading to record high V_{br}.[93] The channel of the β-Ga_2O_3 MOSFET is composed a 150-nm-thick Si-doped (1.5 × 10^{18} cm^{-3}) β-Ga_2O_3 epitaxial layer grown on a Fe-doped (010) β-Ga_2O_3 substrate by MBE. Since the channel doping concentration is high enough, there is no need for the area-selective Si-ion implantation at the S/D regions. Such a design has also been seen in other β-Ga_2O_3 MOSFETs.[87,88] The MOSFET with the optimized field-plate design (L_{FP} = 3 μm and L_{GD} = 25 μm) can achieve V_{br} = 2321 V in Fluorinert, but relatively large $R_{on,sp}$ = 959 mΩ cm^2 and thus relatively low PFOM = 5.6 MW cm^{-2} (Table 4H).[93]

Recessed Gates and Heterostructure FETs. To further decrease $R_{on,sp}$ while maintaining high V_{br}, in 2019, Tetzner et al. demonstrated depletion-mode β-Ga_2O_3 MOSFETs featuring sub-μm gate length and gate recess for low $R_{on,sp}$ and SiN_x internal passivation for high V_{br} (Figure 3C).[94] The channel region is composed of a 200-nm-thick Si-doped β-Ga_2O_3 layer homoepitaxially grown on an Mg-doped (100) β-Ga_2O_3 substrate with a 6° miscut toward the $[00\bar{1}]$ direction. The miscut angle was for avoiding the formation of twin lamellae.[62] The 100-nm-deep recessed gate was lithographically structured by using BCl_3 reactive ion etching (RIE), followed by atomic layer deposition (ALD) of 25-nm-thick Al_2O_3 gate dielectric. The device isolation was carried out by a multiple energy N-ion implantation. The β-Ga_2O_3 MOSFET with the L_{GD} = 10 μm can achieve V_{br} = 1830 V, $R_{on,sp}$ = 21.6 mΩ cm^2, and record high PFOM = 155 MW cm^{-2} (Table 4I).[94] Despite the high breakdown electric field of β-Ga_2O_3 (8 MV cm^{-1}) which enables high V_{br}, most β-Ga_2O_3 MOSFETs suffer from large $R_{on,sp}$, especially when the gate-drain distance needs to be long for reducing the peak electric field. Considering the relatively low intrinsic electron mobility of β-Ga_2O_3 (estimated 100−300 cm^2 V^{-1} s^{-1}) compared to SiC and GaN (Table 1), the heterostructure FETs with two-dimensional electron gas (2DEG) channels can achieve high channel mobility due to the absence of impurity scattering.[95,96] In 2019, Joishi et al. demonstrated β-$(Al_{0.22}Ga_{0.78})_2O_3/Ga_2O_3$ modulation-doped heterostructure FETs with gate-connected field-plates and SiN_x passivation layers (Figure 3D).[97] The device epitaxial layers comprise a 100 nm UID β-Ga_2O_3 buffer layer, a 5 nm β-$(Al_{0.22}Ga_{0.78})_2O_3$ spacer, a delta sheet of Si dopants, and a 25 nm β-$(Al_{0.22}Ga_{0.78})_2O_3$ barrier, all grown on a Fe-doped (010) β-Ga_2O_3 substrate by PA-MBE. The temperature dependent Hall measurements indicated that the charge density of the conducting channel, mainly composed of the 2DEG, is 3.4 × 10^{12} cm^{-2} with the electron mobility equal to 101 cm^2 V^{-1} s^{-1}, which is comparable to the electron mobility achieved by the Ge-doped β-Ga_2O_3 channels (111 cm^2 V^{-1} s^{-1}).[87] It is worth mentioning that similar β-$(Al_xGa_{1-x})_2O_3/\beta$-$Ga_2O_3$ modulation-doped heterostructure FETs with a delta sheet of Ge dopants has also been demonstrated.[98] The field-plate design with SiN_x internal passivation is expected to yield higher V_{br}, because the SiN_x exhibits a (dielectric constant, ϵ_r) × (dielectric strength, kV mm^{-1}) product of 75 MW cm^{-1}, which is higher than SiO_2 (39 MW cm^{-1}) and Al_2O_3 (69.4 MW cm^{-1}).[99,100] The β-$(Al_{0.22}Ga_{0.78})_2O_3/Ga_2O_3$ modulation-doped heterostructure FET with the L_{GD} = 16 μm can achieve V_{br} = 1365 V, $R_{on,sp}$ = 120.1 mΩ cm^2, and PFOM = 15.5 MW cm^{-2} (Table 4K).[97]

Ohmic Contact Formation. On the aspect of reducing $R_{on,sp}$, one primary task is to form high-quality ohmic contacts at the S/D regions. The commonly used metallization schemes on the β-Ga_2O_3 epitaxial layers include Ti/Au and Ti/Al/Ni/Au, followed by post-metallization annealing at 400−500 °C in nitrogen.[13] The physical mechanisms for the ohmic contact formation between Ti/Au and Sn-doped β-Ga_2O_3 were investigated.[101] It was found that at the junction between Ti and β-Ga_2O_3, a thin layer of Ti-TiO_x, which is partially lattice matched to the β-Ga_2O_3, can facilitate electron transport. Furthermore, the interdiffusion between Au and Ti can narrow the distance between the low-resistance Au and heavily doped β-Ga_2O_3.[101] In addition to the metallization and annealing, high doping concentrations at the S/D regions are also critical to reduce the contact resistance. The commonly used doping methods include Si-ion implantation and Sn-doped spin-on-glass (SOG).[102,103] After Si-ion implantation with the concentration 10^{19}−10^{20} cm^{-3}, the implanted β-Ga_2O_3 substrates were annealed at 900−1000 °C in nitrogen to achieve a high activation efficiency of more than 60%. With the annealed Ti/Au electrodes, the specific contact resistance can be as low as 4.6 × 10^{-6} Ω cm^2.[102] In another MOSFET work, the Ti/Au contacts (annealed at 470 °C in nitrogen for 1 min after metallization) on top of a Si-ion implanted S/D regions (Si = 5 × 10^{19} cm^{-3}, annealed at 925 °C in nitrogen for 30 min after implantation) can achieve a similar specific contact resistance of 8.1 × 10^{-6} Ω cm^2.[85] On the other hand, for the SOG doping, the S/D regions were first spin-coated with a 170-nm-thick layer of SOG (Sn = 4 × 10^{21} cm^{-3}), followed by a 5 min and 1100 °C annealing process in nitrogen for the Sn ions to diffuse into the β-Ga_2O_3 layer. Lastly, the SOG layer was removed by a pH-buffered HF treatment.[103] The Sn doping concentration is 4 × 10^{21} cm^{-3} at the surface and decays exponentially with the depth into the β-Ga_2O_3 layer. Combined with the annealed Ti/Au electrodes, the specific contact resistance is 2.1 × 10^{-5} Ω cm^2, which is much higher than the contact resistance achieved by the Si-ion implantation method. This could be part of the reason why the β-Ga_2O_3 MOSFETs with the SOG S/D contacts have relatively high $R_{on,sp}$ and relatively low PFOM (Table 4E and F).[89,103] Recently, Jeong et al. demonstrated that by using CF_4 plasma treatment, an ohmic contact can be formed between the Ti/Al/Ti electrode and the Si-doped β-Ga_2O_3 epitaxial layer grown on a *c*-plane sapphire substrate by HVPE (Table 4J).[104] The CF_4 plasma treatment was performed by using a reactive ion etcher with the RF power of 150 W and the slow introduction of CF_4 and O_2 gases into the chamber filled with nitrogen. Then, the Ti/Al/Ti metal stacks at the S/D regions were formed by evaporation, and the deposited electrodes are ohmic even without post-metallization annealing. However, the resulting specific contact resistance (2 × 10^{-3} Ω cm^2) remains relatively high.[104]

Recessed Gates and Self-Aligned Gates for RF Operation. So far, the high-breakdown electric field of β-Ga_2O_3 (8 MV cm^{-1}) has been mainly applied toward the

https://doi.org/10.1021/acsomega.2c03345
ACS Omega 2022, 7, 36070−36091

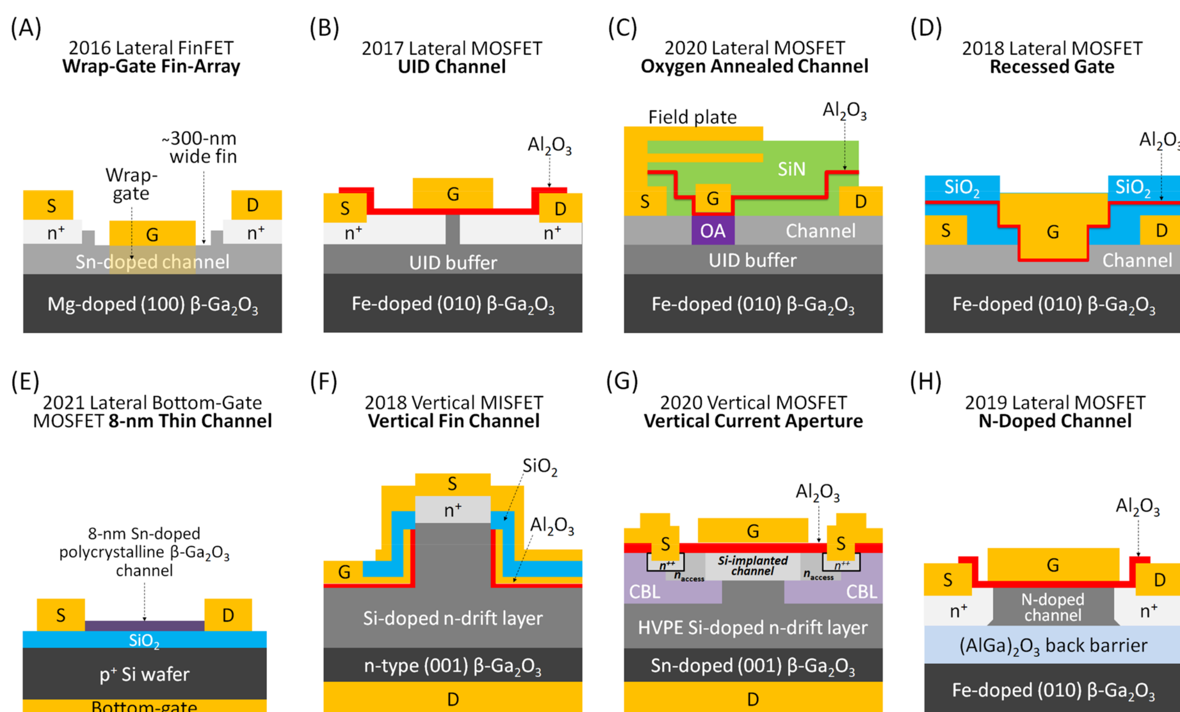

Figure 4. Cross-section illustrations of representative enhancement-mode β-Ga_2O_3 FETs, including (A) FinFET with a wrap-gate,[112] (B) MOSFET with a narrow UID channel,[113] (C) MOSFET with an oxygen annealed channel and double source-connected field-plates,[114] (D) MOSFET with a recessed gate,[115] (E) bottom-gate MOSFET with an 8-nm-thin channel,[116] (F) MISFET with a vertical fin channel,[117] (G) MOSFET with a vertical current aperture,[118] and (H) MOSFET with a N-doped channel.[122]

power switching application, for which the power device performance is evaluated by the PFOM = $V_{br}^2/R_{on,sp}$ (Table 4). On the other hand, the high breakdown electric field of β-Ga_2O_3 is also advantageous in the JFOM = (breakdown electric field) × (electron saturation velocity),[83] which describes the power-frequency product for the RF applications, such as RF amplifiers, RF switches, and power switching at GHz speed. Based on the combination of ab initio calculations and full band Monte Carlo simulations, a peak electron saturation velocity of 2×10^7 cm s^{-1} is estimated at an electric field of 200 kV cm^{-1} (Table 1).[105] Therefore, the JFOM of β-Ga_2O_3 can be higher than GaN and SiC (Table 1). In light of this, in 2017, Green et al. demonstrated depletion-mode β-Ga_2O_3 MOSFETs with recessed gates for small- and large-signal RF operations (Figure 3E).[106] The epitaxial layers, including a 180-nm-thick Si-doped channel layer (1×10^{18} cm^{-3}) and a 25-nm-thick Si-doped ohmic layer (1×10^{19} cm^{-3}), were grown on a (100) β-Ga_2O_3 substrate with a 6° miscut by MOCVD, followed by multiple steps of lithographic RIE for the mesa device isolation and the formation of S/D regions and recessed gate. For the DC operation, the β-Ga_2O_3 MOSFET exhibits maximum current density = 150 mA mm^{-1} and maximum transconductance (g_m) of 21.2 mS mm^{-1} at V_{GS} = −3.5 V and V_{DS} = 40 V. For the small-signal RF operation, the same device exhibits cutoff frequency (f_T) and maximum oscillating frequency (f_{MAX}) equal to 2.7 and 12.9 GHz, respectively, at the DC biasing condition of maximum g_m. For the large-signal CW RF operation, the same device achieves output power (P_{OUT}) of 0.23 W mm^{-1} with power added efficiency (PAE) of 6.3% at 800 MHz using passive source and load tuning.[106] In 2019, Liddy et al. demonstrated depletion-mode β-Ga_2O_3 MOSFETs with self-aligned refractory metal gates (SAGs) for eliminating the source access resistance (Figure 3F).[107] The device fabrication started with the depositions of a 22-nm-thick Si-doped β-Ga_2O_3 epitaxial layer on a Fe-doped (010) β-Ga_2O_3 substrate by MOCVD and then a 30-nm-thick Al_2O_3 gate dielectric by ALD, which can also serve as the implant cap. Next, the W/Cr gate electrode was formed by sputtering and lithographic RIE, followed by Si-ion implantation to define the S/D regions. Lastly, after removing the Al_2O_3 implant cap, the annealed Ti/Al/Ni/Au metals stacks formed ohmic contacts to the implanted regions. Due to the negligible source access resistance and the short channel length (2.5 μm), the β-Ga_2O_3 MOSFET achieves maximum g_m of 35 mS mm^{-1} at V_{GS} = 4 V and V_{DS} = 10 V.[107]

Delta-Doped Channels and Oxygen Annealed UID Layers for RF Operation. For the power devices operating at high frequencies, the gate length usually needs to be scaled into the sub-μm regime. However, such a small-sized gate would not be able to effectively control the channel if the channel thickness is higher than 200 nm. Therefore, approaches like recessed gates and thin channels with heavy doping have been adopted to alleviate this issue.[93,94,106] In 2019, Xia et al. demonstrated β-Ga_2O_3 metal−semiconductor FETs (MESFETs) with delta-doped channels for RF operations (Figure 3G).[108] A submonolayer of Si-ion dopants was implanted between two UID buffer layers, which were sequentially grown on a Fe-doped (010) β-Ga_2O_3 substrate by PA-MBE. Based on Hall measurements on an isolated van der Pauw structure, the delta-doped channel has a sheet electron density of 1.13×10^{13} cm^{-2} with the electron mobility equal to 70 cm^2 V^{-1} s^{-1}. The β-Ga_2O_3 MOSFET can achieve maximum g_m of 44 mS mm^{-1} at V_{GS} = 2 V and V_{DS} = 12 V, and record high f_T = 27 GHz and f_{MAX} = 16 GHz.[108] In order to further improve the large-signal RF performance, it is critical to avoid current collapse at high

https://doi.org/10.1021/acsomega.2c03345
ACS Omega 2022, 7, 36070−36091

Table 5. Representative Enhancement-Mode β-Ga_2O_3 FETs with Various Device Structures and Fabricated by Different Deposition Techniques[a]

	Enhancement-Mode β-Ga_2O_3 FETs									
	Features	Substrates/Gates Dielectric	Epitaxial Layers	Carrier Concentrations	V_{br} (V)	$R_{on,sp}$ (mΩ cm^2)	$V_{br}^2/R_{on,sp}$ (MW cm^{-2})	$I_{ds,sat}$	I_{on}/I_{off}	ref
(A)	• Lateral finFET • Wrap-gate fin-array	Mg-doped (100) β-Ga_2O_3/20 nm Al_2O_3	• MOCVD • 0.30 μm Sn-doped channel, followed by RIE with Cr hard mask to form fin-array	• Fin-array: 2.3 × 10^{17} cm^{-3}	612 (V_{GS} = 0 V) (L_{SD} = 21 μm) (W_G −19 μm)	∼1.6 (V_{GS} = 4 V) (L_{SD} = 4 μm) (W_G −19 μm)	NR	>∼0.18 mA mm^{-1} (V_{GS} = 4 V) (L_{SD} = 4 μm) (W_G −19 μm)	>10^5	2016[112]
(B)	• Lateral MOSET • UID channel • Si implantation for S/D and access regions	Fe-doped (010) (β-Ga_2O_3/50 nm Al_2O_3	• OA-MBE • 1.20 μm UID buffer layer	• Channel: <4 × 10^{-14} cm^{-3} • S/D: 5 × 10^{19} cm^{-3}	∼40 (V_{GS}= 0 V) (L_{SD}= 4 μm)	∼22.5 (V_{GS} = 38 V) (L_{SD} ∼ 4 μm)	∼7.1 × 10^{-2}	1.4 mA mm^{-1} (V_{GS}= 38 V) (L_{SD} −4 μm)	∼10^6	2017[113]
(C)	• Lateral MOSET • Oxygen annealing treated channel • Double source-connected field-plates • Fluorinert Immersion	Fe-doped (010) β-Ga_2O_3/30 nm Al_2O_3	• MOCVD • 0.20 μm Si-doped channel • 0.60 μm UID buffer layer	• Channel (without oxygen annealing): 2 × 10^{17} cm^{-3}	>3000 (V_{GS} = 0 V) (L_{GD} −17 μm)	163 (V_{GS} = 9 V) (L_{GD}− 17 μm)	>55.2	6.4 mA mm^{-1} (V_{GS} = 9 V) (L_{GD} = 17 μm)	∼10^8	2020[114]
(D)	• Lateral MOSFET • 1-μm-long and recessed gate	Fe-doped (010) β-Ga_2O_3/20 nm SiO_2	• OA-MBE • 0.20 μm Si-doped channel • 0.14 pm recess depth	• Channel: >5.5 × 10^{17} cm^{-3}	505 (V_{GS} = 0 V) (L_{SD} = 8 μm)	17.2 (V_{GS} = 8 V) (L_{SD} = 8 μm)	14.8	∼40 mA mm^{-1} (V_{GS} = 8 V) (L_{SD} = 8 μm)	∼10^9	2018[115]
(E)	• Lateral bottom-gate MOSFET • 8-nm-thick Sn-doped polycrystalline channel	Si+/300 nm SiO_2	• RF sputtering → 900 °C for 1 h in open air → SOG doping • 8 nm Sn-doped channel	• Channel: ∼ 1.7 × 10^{17} cm^{-3}	224 (V_{GS} − V_{TH} = −70 V)	1.8 × 10^7 (V− V_{TH} = 90 V)	2.8 × 10^{-6}	∼15 nA mm $^{-1}$ (V_{GS} − V_{TH} = 90 V)	∼10^3	2021[116]
(F)	• Vertical MISFET • Low carrier concentration in the n-drift region	n-type (001) β-Ga_2O_3/30 nm Al_2O_3	• HVPE • 10 μm Si-doped n-drift region	• Source region: 5 × 10^{19} cm^{-3} • n-drift region: <2 × 10^{16} cm^{-3} • Substrate: 2 × 10^{18} cm^{-3}	1057 (V_{GS} = 0 V)	∼18 (V_{GS} = 3 V) (Source Area = 0.33 μm × 80 μm)	∼62.1	∼350 A cm^{-2} (V_{GS} = 3 V) (Source Area = 0.33 μm × 80 μm)	∼10^8	2018[117]
(G)	• Vertical MOSFET • N-ion implanted CBLs to form vertical current apertures	Sn-doped (001) β-Ga_2O_3/50 nm Al_2O_3	• HVPE • 9 μm Si-doped n-drift region	• Source region: 5 × 10^{19} cm^{-3} • Channel: 5 × 10^{17} cm^{-3} • n-drift region: 1.5 × 10^{16} cm $^{-3}$ • Substrate: 3 × 10^{18} cm^{-3}	263 (V_{GS} = 0 V)	135 (V_{GS} = 6 V)	0.5	26 A cm^{-2} (V_{GS} = 6 V)	2 × 10^7	2020[118]
(H)	• Lateral MOSFET • N-doped p-type channel	Fe-doped (010) β-Ga_2O_3/20 nm Al_2O_3	• PA-MBE • 50 nm N-doped p-type UID channel • 100 nm $(AlGa)_2O_3$ back barrier layer	• Channel: N: 1 × 10^{18} cm^{-3}; O: 2 × 10^{17} cm^{-3} • S/D: 5 × 10^{19} cm^{-3}	NR	NR	NR	1.2 μA mm^{-1} (V_{GS} = 8 V) (L_G − L_{SD} = 4 μm)	>10^5	2019[122]

[a].For each power device, the parameters for evaluating the power switching performance are summarized, including the three-terminal off-state breakdown voltage (V_{br}), on-resistance normalized by the device area ($R_{on,sp}$), power figure of merit (PFOM = $V_{br}^2/R_{on,sp}$), maximum saturation drain current ($I_{ds,sat}$) and I_{on}/I_{off} ratio.

https://doi.org/10.1021/acsomega.2c03345
ACS Omega 2022, 7, 36070−36091

drain bias (V_{DS}). Therefore, a UID buffer layer is always needed to keep the channel away from the Fe- or Mg-doped insulating substrate. However, background donors, such as Si or hydrogen or oxygen vacancies due to imperfect epitaxy, may lead to a background electron concentration 10^{15}−10^{16} cm^{-3}. To resolve the issue of conductive UID layers, in 2020, Lv et al. applied an oxygen annealing process for compensating and neutralizing the donors in the UID layer (Figure 3H).[109] After the epitaxial growth of a 0.2-μm-thick Si-doped channel and a 0.5-μm-thick UID buffer layer and the formation of ohmic contacts at the S/D regions, the channel region was deposited with a 0.2-μm-thick SiN passivation layer by plasma-enhanced CVD (PECVD), followed by lithographic etching to expose the gate foot region for the oxygen annealing process (500 °C for 5 min in oxygen atmosphere). The β-Ga_2O_3 MOSFET with the oxygen annealing treatment can achieve maximum g_m of 11 mS mm^{-1} at V_{GS} = 10 V and V_{DS} = 20 V, and f_T = 1.8 GHz, f_{MAX} = 4.2 GHz, P_{OUT} = 0.4 W mm^{-1}, and PAE = 10% for the large-signal CW RF operation at 1 GHz.[109]

ENHANCEMENT-MODE β-Ga_2O_3 FETS

For mitigating off-state power loss and ensuring safe operation at high voltages, normally off enhancement-mode transistors are usually preferable to depletion-mode transistors, which require a negative V_{GS} to remain in the off-state. Several approaches have been investigated to shift the threshold voltage (V_{TH}) from negative to positive, as discussed below.

Nonplanar Fin-Shaped Channels. As revealed by the GaN and AlGaN nanowire fin-shaped FETs (finFETs), the metal gate wrapping around the fins can partially or fully deplete the channels with enhanced electrostatics.[110,111] Following this concept, in 2016, Chabak et al. demonstrated β-Ga_2O_3 wrap-gate finFETs capable of normally off operation with the V_{TH} between 0 and 1 V (Figure 4A).[112] The fabrication of the β-Ga_2O_3 fin-array started on a 300-nm-thick Sn-doped β-Ga_2O_3 epitaxial layer grown on a Mg-doped (100) β-Ga_2O_3 substrate by MOCVD, and then Cr hard mask arrays of ∼300-nm-wide fin channels separated with ∼900 nm pitch were formed on the β-Ga_2O_3 epitaxial layer by electron beam lithography (EBL) and metal evaporation. Subsequently, a RIE step using BCl_3 chemistry, with the etching selectivity Ga_2O_3:Cr ≈ 2:1, removed the entire Cr mask while creating triangular-shaped fins. The β-Ga_2O_3 wrap-gate finFET with the L_{SD} = 4 μm and L_G = 2 μm can achieve a I_{on}/I_{off} ratio larger than 10^5 but only a very limited $I_{ds,sat}$ of ∼0.18 mA mm^{-1}. With the L_{GD} increased to 21 μm, the V_{br} can be as large as 612 V at V_{GS} = 0 V (Table 5A).[112]

UID or Oxygen Annealed Channels. Compared to the complex fin-shaped channels, in 2017, Wong et al. demonstrated that by using a relatively simple, 4-μm-long UID channel defined by Si-ion implantation, enhancement-mode β-Ga_2O_3 MOSFETs with positive V_{TH} can be realized (Figure 4B).[113] Following the deposition of a 1.2-μm-thick UID buffer layer on a Fe-doped (010) β-Ga_2O_3 substrate by OA-MBE, the S/D regions as well as the access regions were formed by Si-ion implantation (5 × 10^{19} cm^{-3}), leaving a 4 μm undoped gap as the channel region. The background electron concentration was estimated to be less than 4 × 10^{14} cm^{-3} by C−V analysis on a Schottky barrier diode (SBD) comprising Pt/β-Ga_2O_3 UID. The β-Ga_2O_3 MOSFET can achieve an I_{on}/I_{off} ratio nearly 10^6 and a decent $I_{ds,sat}$ = 1.4 mA mm^{-1}. However, the V_{br} is only ∼40 V, which is attributed to premature breakdown through the Al_2O_3 dielectric layer between the gate and drain (Table 5B).[113] Previously, an oxygen annealing process was applied for compensating and neutralizing the background donors in the UID layer, in order to improve the MOSFET's large-signal RF performance (Figure 3H).[109] Following the same concept, in 2020, Lv et al. demonstrated that the oxygen annealing treatment under the gate region can exhaust the electron concentration in the channel, leading to normally off operation (Figure 4C).[114] A 0.6-μm-thick UID buffer layer and a 0.2-μm-thick Si-doped (2 × 10^{17} cm^{-3}) channel layer were epitaxially grown on a Fe-doped (010) β-Ga_2O_3 substrate by MOCVD. After the formation of ohmic contacts at the S/D regions, a 0.2-μm-thick SiN was deposited via PECVD, followed by lithographic etching to expose the gate foot region for the oxygen annealing process (500 °C for 5 min in oxygen atmosphere). The β-Ga_2O_3 MOSFET with the double source-connected field-plates and L_{GD} = 17 μm can achieve record high V_{br} > 3000 V in Fluorinert FC-770, $R_{on,sp}$ = 163 mΩ cm^2, and PFOM > 55.2 MW cm^{-2} (Table 5C).[114]

Recessed Gates or Ultrathin Channels. As described previously, small-sized and recessed gates are useful in rapidly controlling the channels for RF operations.[94,106] In 2018, Chabak et al. demonstrated that if the active channel thickness, decreased by the recessed gate, is small enough, the gated region of the channel can be fully depleted at V_{GS} = 0 V (Figure 4D).[115] The channel, a 0.2-μm-thick Si-doped β-Ga_2O_3 epitaxial layer, was grown on a Fe-doped (010) β-Ga_2O_3 substrate, followed by a similar recessed gate formation process as described previously.[106] The recess depth was ∼140 nm, leaving the active channel thickness of ∼60 nm in the gated region. Based on Hall measurements on several unetched van der Pauw structures, the undepleted channel layer has an average minimum free carrier concentration of 5.5 × 10^{17} cm^{-3} and an average sheet electron mobility of 106 cm^2 V^{-1} s^{-1}. The enhancement-mode β-Ga_2O_3 MOSFET, with the recessed gate design, L_G = 1 μm and L_{SD} = 8 μm, can achieve V_{br} = 505 V, $R_{on,sp}$ = 17.2 mΩ cm^2, and PFOM = 14.8 MW cm^{-2} (Table 5D).[115] Following the concept of applying an ultrathin, fully depleted channel for enhancement-mode FETs, in 2021, Yoon et al. demonstrated that 8-nm-thin Sn-doped polycrystalline β-Ga_2O_3 thin films can serve as the channels of bottom-gate MOSFETs capable of normally off high-voltage operation (Figure 4E).[116] The device fabrication started with the deposition of an amorphous 8 nm thin Ga_2O_3 thin film on a SiO_2/p+ Si substrate by RF sputtering, followed by annealing at 900 °C for 1 h in an open atmosphere for crystallization into monoclinic β-Ga_2O_3. The n-type doping of the β-Ga_2O_3 thin film was accomplished by a similar SOG method as described previously.[102,103] Finally, the S/D electrodes were formed by the deposition of Ti/TiN metal stacks by RF sputtering. The optical bandgap of the 8-nm-thin Sn-doped polycrystalline β-Ga_2O_3 thin film (5.77 eV) is higher that of a 100-nm-thick β-Ga_2O_3 thin film (4.7 eV) due to the quantum confinement effect. The back-gate MOSFET with the nanomembrane channel can achieve high V_{br} = 224 V, but the $R_{on,sp}$ and $I_{ds,sat}$ are unsatisfactory compared to conventional β-Ga_2O_3 FETs fabricated by epitaxy (Table 5E).[116]

Vertical Fins or Current Apertures. In 2018, Hu et al. demonstrated high-voltage, vertical β-Ga_2O_3 MOSFETs which can remain in the off-state with V_{GS} = 0 V under V_{DS} > 1 kV (Figure 4F).[117] A 10-μm-thick Si-doped (N_d < 2 × 10^{16} cm^{-3}) n-drift layer was grown on an n-type (001) β-Ga_2O_3 substrate by HVPE, followed by Si-ion implantation (N_d = 5 × 10^{19} cm^{-3}) on the epitaxial layer to form the source region. Then,

https://doi.org/10.1021/acsomega.2c03345
ACS Omega 2022, 7, 36070−36091

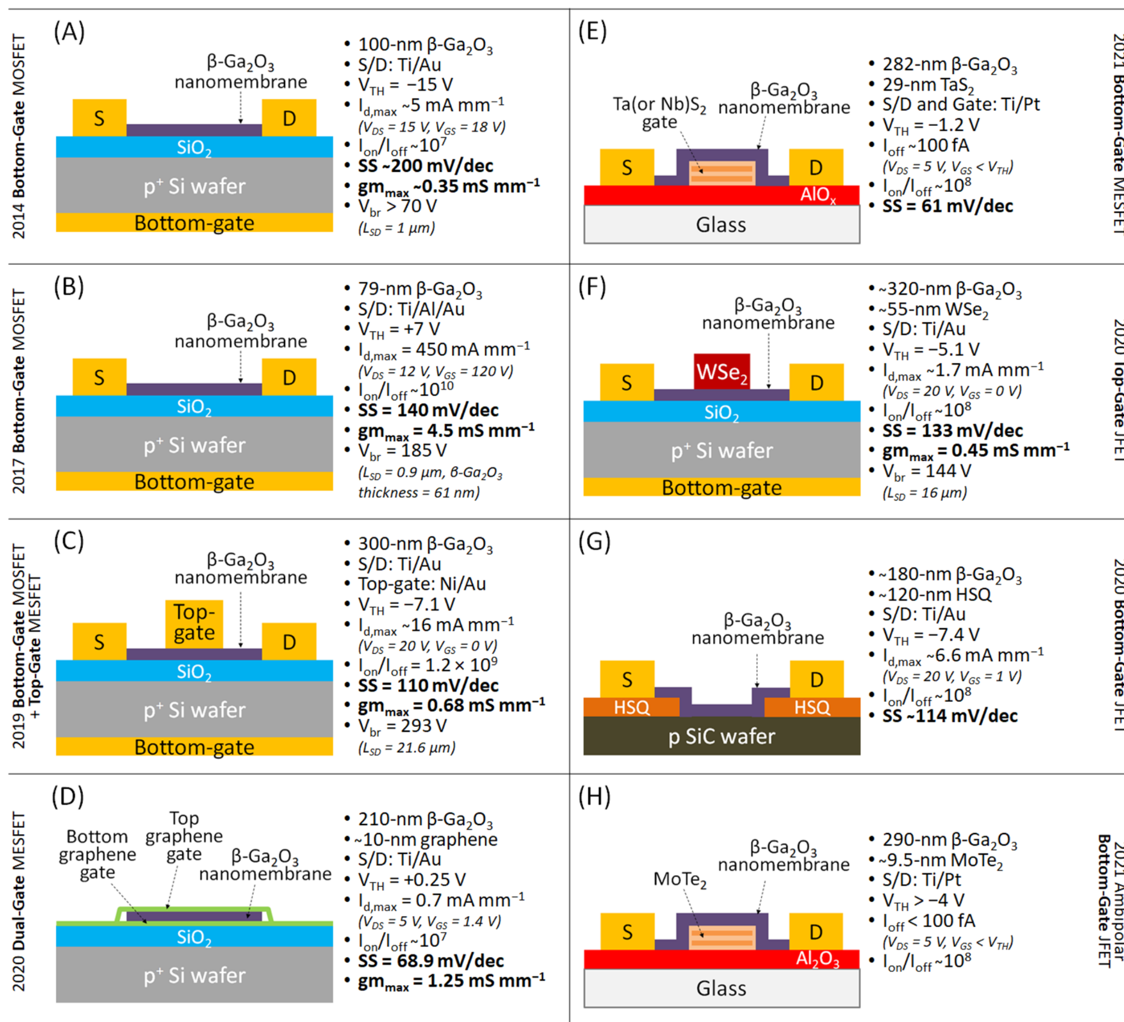

Figure 5. Schematic drawings of representative β-Ga_2O_3 nanomembrane FETs with various gating schemes, including (A, B) bottom-gate MOSFETs,[123,127] (C) bottom-gate MOSFET and top-gate MESFET,[132] (D) dual-gate MESFET,[133] (E) bottom-gate MESFET,[134] (F) top-gate JFET,[135] (G) bottom-gate JFET,[137] and (H) ambipolar bottom-gate JFET.[138] For each β-Ga_2O_3 nanomembrane FET, the parameters for evaluating the device performance are summarized, including the threshold voltage (V_{TH}), maximum drain current ($I_{d,max}$), I_{on}/I_{off} ratio, subthreshold slope (SS), maximum transconductance (gm_{max}), and breakdown voltage (V_{br}).

the vertical channel was formed by RIE with the patterned Pt metal mask which defines the position and area of the source. A 30-nm-thick Al_2O_3 was deposited by ALD as the gate dielectric, followed by sputtering a 50-nm-thick Cr as the gate electrode. The vertical β-Ga_2O_3 MOSFET with the source area equal to 0.33 μm × 80 μm can achieve V_{br} = 1057 V at V_{GS} = 0 V and $R_{on,sp}$ ~ 18 mΩ cm^2, resulting in PFOM ~ 62.1 MW cm^{-2} (Table 5F).[117] Following the concept of vertical fin channel, in 2020, Wong et al. used N-ion implanted current blocking layers (CBLs) to form vertical current apertures connecting between drain and source (Figure 4G).[118] A 9-μm-thick Si-doped (1.5 × 10^{16} cm^{-3}) n-drift layer was formed on a Sn-doped (001) β-Ga_2O_3 substrate by HVPE, followed by chemical mechanical polishing. The 0.8-μm-thick CBLs were formed in the epitaxial layer by N-ion implantation (1.5 × 10^{18} cm^{-3}), followed by annealing at 1100 °C for 30 min in nitrogen to remove implantation damage and activate the implanted N as compensating acceptors. Subsequently, Si-ion implantation was conducted to form the channel regions, source access regions, and source contact layers, with the doping concentrations equal to 5 × 10^{17} cm^{-3}, 2 × 10^{18} cm^{-3}, and 5 × 10^{19} cm^{-3}, respectively, followed by annealing at 950 or 800 °C for 30 min in nitrogen for the donor activation. The vertical β-Ga_2O_3 MOSFET with the CBL formed vertical current aperture can achieve V_{br} = 263 V at V_{GS} = 0 V and $R_{on,sp}$ = 135 mΩ cm^2, resulting in PFOM = 0.5 MW cm^{-2} (Table 5G).[118]

N-Doped p-Type Channel. Theoretically, N can act as deep acceptors in β-Ga_2O_3,[119−121] while Si has been experimentally confirmed as shallow donors. In 2019, Kamimura et al. demonstrated that by controlling the doping concentration ratio between N and Si, the β-Ga_2O_3 UID layer can behave as a p-type channel, based on which an enhancement-mode β-Ga_2O_3 MOSFET can be obtained (Figure 4H).[122] The device was based on a 50-nm-thick UID channel layer and a 100-nm-thick $(AlGa)_2O_3$ back barrier layer, both of which were grown on a Sn-doped (010) β-Ga_2O_3 substrate by PA-MBE, with the Ga beam flux constantly at 1.8 × 10^{-7} Torr and the O_2 flux at ~1 sccm, that is around the stoichiometry condition. According to the secondary ion mass spectroscopy (SIMS) analysis, in the UID channel the N concentration (1 × 10^{18} cm^{-3}) was estimated to be much

https://doi.org/10.1021/acsomega.2c03345
ACS Omega 2022, 7, 36070−36091

higher than the Si concentration (2×10^{17} cm^{-3}), making the UID channel p-type. The enhancement-mode β-Ga_2O_3 MOSFET with the p-type UID channel and the V_{TH} > +8 V can achieve a I_{on}/I_{off} ratio larger than 10^5, but the $I_{ds,sat}$ remained low at 1.2 μA mm^{-1}, since the V_{GS} swing was limited up to +8 V by the Al_2O_3 gate leakage (Table 5H).[122]

β-GA_2O_3 NANOMEMBRANE FETS

Despite its UWBG (4.9 eV) and high breakdown electric field (8 MV cm^{-1}), one obvious drawback of β-Ga_2O_3 is the relatively low thermal conductivity (21 W m^{-1} K^{-1} in [010]), compared to Si (150 W m^{-1} K^{-1}), SiC (270 W m^{-1} K^{-1}), and GaN (210 W m^{-1} K^{-1}) (Table 1). In 2014, Hwang et al. found that β-Ga_2O_3 nanomembranes can be easily synthesized by an exfoliation process similar to that of graphene and transferred to a different semiconductor platform.[123] Although β-Ga_2O_3 is not a layered material like graphene, the ease of exfoliation is likely attributed to the monoclinic structure and the higher lattice parameter along the [100] direction than the [010] and [001] directions.[14] The integration scheme is beneficial for on-chip power management and enables the formation of heterojunctions, which may open the possibilities of new (opto) electronic applications. Particularly, in contrast to the low power switching applications demonstrated by other nanomaterials, such as graphene, MoS_2, and WSe_2,[124−126] the β-Ga_2O_3 nanomembrane FETs aim at achieving high-power switching in low dimensions.

Shifting from Depletion- to Enhancement-Mode. As mentioned previously, the enhancement-mode power devices enable fail-safe operation and simplify circuit designs at the system level. For the β-Ga_2O_3 nanomembrane FETs, the V_{TH} can be shifted from negative to positive via various approaches. In 2017, Zhou et al. showed that the V_{TH} of bottom-gate MOSFETs (β-Ga_2O_3/SiO_2/p+ Si) can be increased from −120 V to ∼80 V, when the thickness of the β-Ga_2O_3 nanomembrane channel was shrunk from 110 to 50 nm.[127] In 2019, Kim et al. found that by applying remote CF_4 plasma on part of the β-Ga_2O_3 nanomembrane, the V_{TH} of the top-gate MOSFETs can be increased from −7.5 V without the treatment to ∼2 V with the treatment.[128] In 2022, Wang et al. demonstrated that by forming a heterojunction between the p-type SnO and n-type β-Ga_2O_3 nanomembrane, the V_{TH} of the bottom-gate MOSFETs (SnO/β-Ga_2O_3/SiO_2/p+ Si) can be increased from −40 V without SnO to ∼5 V with 12 nm SnO.[129]

Bottom-Gate MOSFETs. To effectively control the channels of the β-Ga_2O_3 nanomembrane MOSFETs, i.e., to decrease the subthreshold slope (SS, mV/dec) of the MOSFET, various gating schemes have been investigated. The most widely used scheme is the bottom-gate MOSFETs,[123,127,130] in which a β-Ga_2O_3 membrane (as the channel), exfoliated from a (−201) bulk β-Ga_2O_3 crystal, is transferred to the surface of a SiO_2 dielectric layer (as the gate dielectric) deposited on a heavily doped Si substrate (as the bottom-gate). The β-Ga_2O_3 nanomembrane firmly adheres to the SiO_2 surface through the bond-free van der Waals force. Subsequently, the S/D regions are defined by EBL, followed by Ti/Al/Au or Ti/Au metallization and a lift-off process. Two representative bottom-gate β-Ga_2O_3 nanomembrane FETs and their electrical characteristics are shown in Figure 5A and B.[123,127] It is worth mentioning that an Ar plasma bombardment process prior to the S/D metallization step can effectively reduce the contact resistance. Without the Ar bombardment, the contacts may show Schottky-like behaviors.[127] Furthermore, to achieve high drain currents, the β-Ga_2O_3 nanomembrane channels need to have adequate electron concentrations. Therefore, heavily doped crystals (2.7×10^{18} cm^{-3}), from which the nanomembranes are exfoliated, are desirable.[127] The bottom-gate β-Ga_2O_3 nanomembrane FETs also exhibit much better temperature and air stabilities, compared to devices based on conventional 2D transition metal dichalcogenides. No degradation of electrical characteristics was observed when the operating temperature was elevated to 250 °C or after a month-long storage in ambient condition.[130] Moreover, the electrical properties of the bottom-gate β-Ga_2O_3 nanomembrane FETs can be improved by Al_2O_3 surface passivation, which reduces surface states and absorbates at the nanomembrane surface.[131]

Dual-Gate FETs. To further enhance the channel control, dual-gate β-Ga_2O_3 nanomembrane FETs have been developed recently.[132,133] In 2019, Ma et al. demonstrated a dual-gate β-Ga_2O_3 nanomembrane FET, comprising a top-gate MESFET and a bottom-gate MOSFET, as shown in Figure 5C.[132] Upon the bottom-gate MOSFET (β-Ga_2O_3/SiO_2/p+ Si), the top-gate electrode (Ni/Au) was deposited over a part of the β-Ga_2O_3 channel by EBL and lift-off processes. A Schottky contact is formed at the Ni/β-Ga_2O_3 interface. Therefore, when a negative potential is applied to the top-gate, the depletion width of the Schottky junction expands, reducing the effective channel thickness. Compared to the bottom-gating mode, the β-Ga_2O_3 nanomembrane FET operating in the dual-gating mode exhibited a positively shifted V_{TH}, a much higher gm_{max}, and a much lower SS.[132] In 2020, Kim et al. demonstrated double graphene-gate β-Ga_2O_3 nanomembrane MESFETs (graphene/β-Ga_2O_3/graphene), as shown in Figure 5D.[133] The graphene and β-Ga_2O_3 nanomembranes were mechanically exfoliated from the pyrolytic graphite and (−201) β-Ga_2O_3 crystals, respectively, and subsequently integrated into the multilayered architecture via van der Waals heterojunctions on a SiO_2/p+ Si substrate. The S/D electrodes were formed by EBL and lift-off processes, followed by a rapid thermal annealing step (1 min in Ar at 480 °C) to form ohmic contacts with the β-Ga_2O_3 channel. Compared to the single graphene-gate device with a negative V_{TH} (−0.96 V), the double graphene-gate β-Ga_2O_3 MESFET operated with a positive V_{TH} (+0.25 V) and achieved a low SS (68.9 mV/dec). The excellent electrical properties are attributed to the high crystallinity of each exfoliated nanomembrane and the high-quality interface between graphene and β-Ga_2O_3.[133]

Bottom-Gate MESFETs. In addition to the Schottky junctions described previously (Ni/β-Ga_2O_3 and graphene/β-Ga_2O_3),[132,133] in 2021, Kim et al. demonstrated bottom-gate nanomembrane MESFETs based on the Schottky junctions of Nb(or Ta)S_2/β-Ga_2O_3, as shown in Figure 5E.[134] The exfoliated Nb(or Ta)S_2 nanoflake as the bottom-gate was dry-transferred onto a AlO_x-coated glass substrate by polydimethylsiloxane (PDMS) stamping. Then the β-Ga_2O_3 nanomembrane channel was precisely aligned and electrostatically transferred onto the Nb(or Ta)S_2 nanoflake. The S/D and gate electrodes (Ti/Pt) were defined by photolithography, sputtering deposition, and lift-off processes. Note that after the UV exposure and development, plasma treatment to the β-Ga_2O_3 was performed for improving the ohmic contacts. Due to TaS_2's larger work function (5.6 eV) than usual novel metals, the TaS_2 bottom-gate β-Ga_2O_3 nanomembrane MESFET achieved a record low (61 mV/dec) with a negative

https://doi.org/10.1021/acsomega.2c03345
ACS Omega 2022, 7, 36070−36091

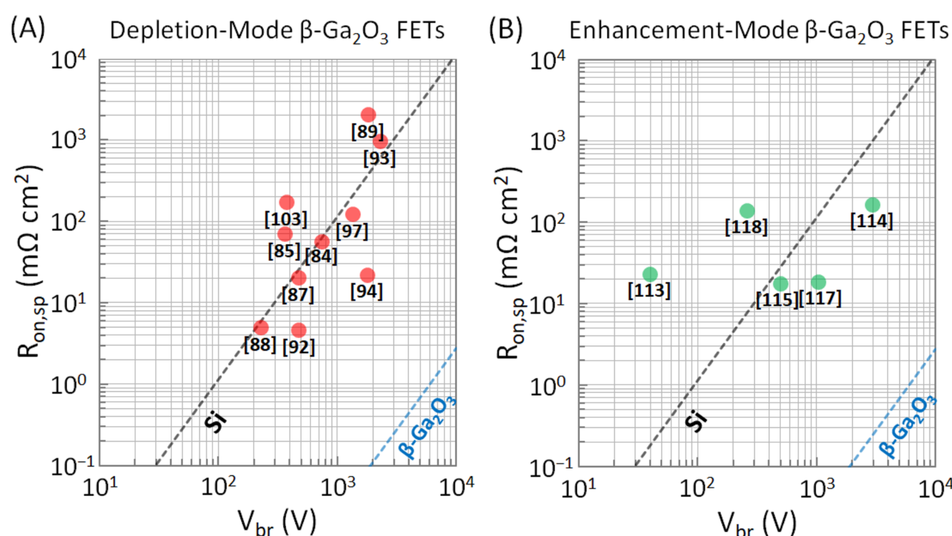

Figure 6. (A) Representative depletion-mode β-Ga_2O_3 FETs with the V_{br} and $R_{on,sp}$ listed in Table 4 (red circles). (B) Representative enhancement-mode β-Ga_2O_3 FETs with the V_{br} and $R_{on,sp}$ listed in Table 5 (green circles). The black and blue dashed lines represent the Baliga's theoretical limits for Si and β-Ga_2O_3, respectively.

V_{TH} (−1.2 V). When integrated as a switch into a green organic LED pixel circuit, the β-Ga_2O_3 nanomembrane MESFET exhibits almost the same or even superior low leakage (~100 fA) performance compared to conventional a-IGZO channel MOSFETs in the pixel switching.[134]

Top-Gate JFETs. By taking advantage of the strain-free van der Waals heterojunctions between the exfoliated β-Ga_2O_3 nanomembranes and other two-dimensional semiconductor nanomaterials, junction FETs (JFETs) of various forms have been developed recently.[135−138] In 2018, Kim et al. demonstrated heterojunction β-Ga_2O_3 nanomembrane JFETs through van der Waals bonding with exfoliated WSe_2 nanomembranes, as shown in Figure 5F.[135] The device fabrication was similar to the graphene/β-Ga_2O_3/graphene dual-gate MESFETs,[133] except that the graphene dual-gate was replaced by a WSe_2 top-gate. The rectifying current−voltage characteristic of the heterojunction comprising p-type WSe_2 and n-type β-Ga_2O_3 was clearly observed. When applied with a negative V_{GS}, the depletion width of the reverse-biased WSe_2/β-Ga_2O_3 heterojunction increases, narrowing the effective channel thickness. The WSe_2 top-gate β-Ga_2O_3 nanomembrane JFET operated in the depletion-mode with the V_{TH} = −5.1 V, SS = 68.9 mV/dec, gm_{max} = 0.45 mS mm^{-1}, and V_{br} = 144 V. Moreover, the JFET exhibited outstanding long-term stability and was able to retain most of the transistor characteristics at high operating temperatures.[135] In 2020, Li et al. demonstrated a similar JFET but with the top-gate replaced by p-type black phosphorus (BP). The BP top-gate β-Ga_2O_3 nanomembrane JFET also operated in the depletion-mode with the V_{TH} = −20 V, SS = 260 mV/dec, and gm_{max} = 4.2 mS mm^{-1}.[136]

Bottom-Gate JFETs. Considering the low thermal conductivity of β-Ga_2O_3, integrating β-Ga_2O_3 nanomembrane FETs on a different material substrate can potentially achieve more efficient on-chip heat dissipation through the substrate. In 2020, Lee et al. demonstrated heterojunction β-Ga_2O_3 nanomembrane JFETs on 4H-SiC substrates through van der Waals bonding, as shown in Figure 5G.[137] The 4H-SiC can function as the bottom-gate as well as the thermal drain due to its relatively high thermal conductivity (Table 1). The device fabrication started with the homoepitaxial growth of a p-type 4H-SiC layer (1 μm thick and doping concentration equal to 2 × 10^{17} cm^{-3}). Then, two hydrogen silsesquioxane (HSQ) covered regions, for insulating the S/D electrodes from the conductive 4H-SiC layer, were formed by EBL, followed by developing using 25% tetramethylammonium hydroxide. An exfoliated β-Ga_2O_3 nanomembrane was dry-transferred onto the HSQ and 4H-SiC to form the channel. Lastly, the S/D electrodes were fabricated by EBL, metallization, and lift-off, followed by rapid thermal annealing for creating ohmic contacts with the β-Ga_2O_3 channel. When applied with a negative V_{GS}, the depletion width of the heterojunction between the p-type 4H-SiC and n-type β-Ga_2O_3 increases, narrowing the effective channel thickness. The 4H-SiC bottom-gate β-Ga_2O_3 nanomembrane JFET operated in the depletion-mode with the V_{TH} = −7.4 V and SS = 114 mV/dec. Most importantly, for the same input power of 160 W m^{-1}, the JFET based on the 4H-SiC substrate exhibited a peak temperature at least 100 °C lower than based on a sapphire substrate, manifesting the stronger heat dissipation of the 4H-SiC substrate.[137] Interestingly, in 2021, Choi et al. demonstrated ambipolar JFETs based on van der Waals heterojunctions formed between exfoliated p-type $MoTe_2$ flakes and exfoliated n-type β-Ga_2O_3 nanomembranes, either of which can function as the channel, as shown in Figure 5H.[138] With the $MoTe_2$ as the bottom-gate and the β-Ga_2O_3 as the channel, the JFET operated in the depletion-mode with the V_{TH} > −4 V and I_{on}/I_{off} ratio ~10^8.[138]

■ CONCLUSION

Due to its UWBG (4.9 eV) and large breakdown electric field (8 MV cm^{-1}), β-Ga_2O_3 has attracted renewed attention as one of the next-generation semiconductors recently. Compared to the commercialized semiconductors, such as Si, GaN, and SiC, power devices based on β-Ga_2O_3 are capable of handling high voltages in smaller dimensions and with higher efficiencies. Furthermore, the β-Ga_2O_3 bulk crystals can be synthesized by the relatively low-cost melt growth methods, such as the FZ, CZ, and EFG methods, making the single-crystal substrates and epitaxial layers readily accessible. Several epitaxy

https://doi.org/10.1021/acsomega.2c03345
ACS Omega 2022, 7, 36070−36091

techniques have been investigated for the depositions of α-, ε-, and β-phase Ga_2O_3, including MOCVD, LPCVD, PA-MBE, HVPE, and mist-CVD, among which MOCVD is most widely used while HVPE offers relatively high growth rates. For the homoepitaxy on the (100) β-Ga_2O_3 substrates, despite ultraflat surfaces obtained, stacking faults in the form of twin lamellae are usually observed in the epitaxial layers, which however can be avoided by using substrates with relatively large miscut angles. In contrast, the epitaxial layers based on the (010) β-Ga_2O_3 substrates possess better crystal qualities, and the heat transfer along the [010] direction is more efficient than along the [100] direction. Therefore, Fe-doped semi-insulating (010) β-Ga_2O_3 substrates are widely used for fabricating high-performance β-Ga_2O_3 MOSFETs. On the other hand, the β-Ga_2O_3 epitaxial layers grown on *c*-plane sapphire substrates, although showing clear (−201)-oriented XRD patterns, are not thoroughly single-crystal, because of the symmetry mismatch between the monoclinic β-Ga_2O_3 and hexagonal Al_2O_3. The orthorhombic ε-Ga_2O_3 can be better matched to the sapphire substrates, but tends to transform into β-Ga_2O_3 upon high-temperature annealing. Therefore, so far the great majority of the β-Ga_2O_3 FETs have been built on the homoepitaxial layers, although heteroepitaxy on the sapphire substrates in the long term should be the more cost-effective solution.

For the power switching application, to exploit the full potential of β-Ga_2O_3, many device-level approaches have been developed to increase V_{br} and decrease $R_{on,sp}$ for maximizing PFOM. The depletion-mode β-Ga_2O_3 FETs with gate- or source-connected field-plates, Fluorinert immersion, and SiN_x passivation can effectively avoid premature breakdown through the β-Ga_2O_3 channel and air, resulting in V_{br} higher than 1000 V. On the aspect of reducing $R_{on,sp}$, the Ge-doped β-Ga_2O_3 channels possess higher electron mobility than the Sn-doped channels, and the 2DEG channels of the heterostructure FETs also exhibit high electron mobility (>100 $cm^2\ V^{-1}\ s^{-1}$) due to the absence of impurity scattering. In addition, ohmic contacts with the channels can be formed via Ti/Au metallization followed by annealing, and the heavily doped S/D regions can be obtained by Si-ion implantation or SOG. As shown in Figure 6A, although some depletion-mode β-Ga_2O_3 FETs have already achieved V_{br} higher than 1000 V, further reduction of $R_{on,sp}$ is necessary, so that the β-Ga_2O_3 FETs' PFOMs can advance closer to the Baliga's theoretical limit. For the RF amplification application, it is desirable for the power devices to have large transconductance gain (gm) and wide bandwidth (f_T and f_{MAX}). To better control the channels, which leads to high gm, recessed gates and delta-doped channels have been applied for the depletion-mode β-Ga_2O_3 FETs, resulting in gm higher than 20 mS mm^{-1}. For increasing the bandwidth, parasitic capacitance and resistance of the β-Ga_2O_3 FETs needs to be minimized. In light of this, the SAGs have been adopted for eliminating the source access resistance.

For mitigating off-state power loss and ensuring safe operation at high voltages, enhancement-mode FETs are usually preferable to depletion-mode ones. Despite the lack of p-type doping, several device-level approaches have been developed to shift the V_{TH} of the β-Ga_2O_3 FETs from negative to positive. The main idea is to deplete the gated region of the channel. For example, the metal wrap-gates of the finFETs can partly or fully deplete the narrow fin channels with enhanced electrostatics. Following the same idea, the enhancement-mode β-Ga_2O_3 FETs with ultrathin channels, recessed gates, vertical fin channels and vertical current apertures have been demonstrated. In addition, the electron concentrations of the channels can be exhausted by using oxygen annealing or by simply adopting an UID channel. It is worth mentioning that p-type UID channels have been demonstrated by using N-ion implantation. However, the drain currents of such devices remained low. Despite the tremendous progress recently, as shown in Figure 6B, the performance of the enhancement-mode β-Ga_2O_3 FETs in general is still lagging the depletion-mode ones in terms of V_{br} and $R_{on,sp}$. Lastly, to resolve the low-thermal conductivity issue of β-Ga_2O_3, exfoliated nano-membranes of β-Ga_2O_3 are integrated into multilayered structures on various semiconductor platforms for better heat dissipation. Based on the strain-free van der Waals heterojunctions which can control the effective channel thickness, the electrical characteristics of the β-Ga_2O_3 nanomembrane FETs can be easily modulated. Depending on the gating schemes, a great variety of β-Ga_2O_3 nano-membrane FETs have been explored, such as bottom-gate MOSFETs (β-Ga_2O_3/SiO_2/p+ Si), top-gate MESFETs (Ni/β-Ga_2O_3), dual-gate MESFETs (graphene/β-Ga_2O_3/graphene), bottom-gate MESFET (β-Ga_2O_3/TaS_2), top-gate JFETs (p-type WSe_2/n-type β-Ga_2O_3 and p-type BP/n-type β-Ga_2O_3), and bottom-gate JFETs (n-type β-Ga_2O_3/p-type SiC and n-type β-Ga_2O_3/p-type $MoTe_2$). In general, the β-Ga_2O_3 nanomembrane FETs possess strong channel control capability, with the SS lower than 200 mV/dec, which is favorable for the high-frequency power switching application. However, the V_{br} and gm of the β-Ga_2O_3 nanomembrane FETs are lower than the epitaxial β-Ga_2O_3 FETs.

■ AUTHOR INFORMATION

Corresponding Authors

Chang-Ching Tu − *Hon Hai Research Institute, Semiconductor Research Center, Taipei 11492, Taiwan;* orcid.org/0000-0002-9233-1928; Phone: +886-3-5643888; Email: chang-ching.tu@foxconn.com

Hao-Chung Kuo − *Department of Photonics, Institute of Electro-Optical Engineering, National Yang Ming Chiao Tung University, Hsinchu 30010, Taiwan; Hon Hai Research Institute, Semiconductor Research Center, Taipei 11492, Taiwan*; Phone: +886-3-5712121 Ext. 31986; Email: hckuo0206@nycu.edu.tw

Ray-Hua Horng − *Institute of Electronics, Ming Chiao Tung University, Hsinchu 30010, Taiwan;* orcid.org/0000-0002-1160-6775; Phone: +886-3-5712121 Ext. 54138; Email: rayhua@nycu.edu.tw

Authors

An-Chen Liu − *Department of Photonics, Institute of Electro-Optical Engineering, National Yang Ming Chiao Tung University, Hsinchu 30010, Taiwan*

Chi-Hsiang Hsieh − *Department of Photonics, Institute of Electro-Optical Engineering, National Yang Ming Chiao Tung University, Hsinchu 30010, Taiwan*

Catherine Langpoklakpam − *Department of Photonics, Institute of Electro-Optical Engineering, National Yang Ming Chiao Tung University, Hsinchu 30010, Taiwan*

Konthoujam James Singh − *Department of Photonics, Institute of Electro-Optical Engineering, National Yang Ming Chiao Tung University, Hsinchu 30010, Taiwan*

Wen-Chung Lee − *Department of Photonics, Institute of Electro-Optical Engineering, National Yang Ming Chiao Tung University, Hsinchu 30010, Taiwan*

https://doi.org/10.1021/acsomega.2c03345
ACS Omega 2022, 7, 36070−36091

Yi-Kai Hsiao − *Hon Hai Research Institute, Semiconductor Research Center, Taipei 11492, Taiwan*

Complete contact information is available at:
https://pubs.acs.org/10.1021/acsomega.2c03345

Author Contributions

[#]A.-C.L. and C.-H.-H. contributed equally.

Notes

The authors declare no competing financial interest.

■ ACKNOWLEDGMENTS

This work was financially supported by the Hon Hai Research Institute, Foxconn Technology Group.

■ REFERENCES

(1) Roy, R.; Hill, V. G.; Osborn, E. F. Polymorphism of Ga_2O_3 and the System Ga_2O_3-H_2O. *J. Am. Chem. Soc.* **1952**, *74*, 719−722.
(2) Geller, S. Crystal Structure of β-Ga_2O_3. *J. Chem. Phys.* **1960**, *33*, 676.
(3) Lorenz, M. R.; Woods, J. F.; Gambino, R. J. Some Electrical Properties of the Semiconductor β-Ga_2O_3. *J. Phys. Chem. Solids* **1967**, *28*, 403−404.
(4) Ueda, N.; Hosono, H.; Waseda, R.; Kawazoe, H. Synthesis and Control of Conductivity of Ultraviolet Transmitting β-Ga_2O_3 Single Crystals. *Appl. Phys. Lett.* **1997**, *70*, 3561.
(5) Tomm, Y.; Reiche, P.; Klimm, D.; Fukuda, T. Czochralski Grown Ga_2O_3 Crystals. *J. Cryst. Growth* **2000**, *220*, 510−514.
(6) Aida, H.; Nishiguchi, K.; Takeda, H.; Aota, N.; Sunakawa, K.; Yaguchi, Y. Growth of β-Ga_2O_3 Single Crystals by the Edge-Defined, Film Fed Growth Method. *J. Jpn. Appl. Phys.* **2008**, *47*, 8506.
(7) Wagner, G.; Baldini, M.; Gogova, D.; Schmidbauer, M.; Schewski, R.; Albrecht, M.; Galazka, Z.; Klimm, D.; Fornari, R. Homoepitaxial Growth of β-Ga_2O_3 Layers by Metal-Organic Vapor Phase Epitaxy. *Phys. Status Solidi A* **2014**, *211*, 27−33.
(8) Gogova, D.; Wagner, G.; Baldini, M.; Schmidbauer, M.; Irmscher, K.; Schewski, R.; Galazka, Z.; Albrecht, M.; Fornari, R. Structural Properties of Si-Doped β-Ga_2O_3 Layers Grown by MOVPE. *J. Cryst. Growth* **2014**, *401*, 665−669.
(9) Tsao, J. Y.; Chowdhury, S.; Hollis, M. A.; Jena, D.; Johnson, N. M.; Jones, K. A.; Kaplar, R. J.; Rajan, S. R.; Walle, C. G. V. d.; Bellotti, E.; Chua, C. L.; Collazo, R.; Coltrin, M. E.; Cooper, J. A.; Evans, K. R.; Graham, S.; Grotjohn, T. A.; Heller, E. R.; Higashiwaki, M.; Islam, M. S.; Juodawlkis, P. W.; Khan, M. A.; Koehler, A. D.; Leach, J. H.; Mishra, U. K.; Nemanich, R. J.; Pilawa-Podgurski, R. C. N.; Shealy, J. B.; Sitar, Z.; Tadjer, M. J.; Witulski, A. F.; Wraback, M.; Simmons, J. A. Ultrawide-Bandgap Semiconductors: Research Opportunities and Challenges. *Adv. Electron. Mater.* **2018**, *4*, 1600501.
(10) Higashiwaki, M. β-Ga_2O_3 Material Properties, Growth Technologies, and Devices: a Review. *AAPPS Bull.* **2022**, *32*, 3.
(11) Bosi, M.; Mazzolini, P.; Seravalli, L.; Fornari, R. Ga_2O_3 Polymorphs: Tailoring the Epitaxial Growth Conditions. *J. Mater. Chem. C* **2020**, *8*, 10975−10992.
(12) Tak, B. R.; Kumar, S.; Kapoor, A. K.; Wang, D.; Li, X.; Sun, H.; Singh, R. Recent Advances in the Growth of Gallium Oxide Thin Films Employing Various Growth Techniques-a Review. *J. Phys. D: Appl. Phys.* **2021**, *54*, 453002.
(13) Pearton, S. J.; Yang, J.; Cary, P. H., IV; Ren, F.; Kim, J.; Tadjer, M. J.; Mastro, M. A. A Review of Ga_2O_3 Materials, Processing, and Devices. *Appl. Phys. Rev.* **2018**, *5*, 011301.
(14) Zhang, H.; Yuan, L.; Tang, X.; Hu, J.; Sun, J.; Zhang, Y.; Zhang, Y.; Jia, R. Progress of Ultra-Wide Bandgap Ga_2O_3 Semiconductor Materials in Power MOSFETs. *IEEE Trans. Power Electron.* **2020**, *35*, 5157−5179.
(15) Higashiwaki, M.; Sasaki, K.; Kuramata, A.; Masui, T.; Yamakoshi, S. Gallium Oxide (Ga_2O_3) Metal-Semiconductor Field-Effect Transistors on Single-Crystal β-Ga_2O_3 (010) Substrates. *Appl. Phys. Lett.* **2012**, *100*, 013504.
(16) Yang, X.; Yu, J.; Chen, X.; Peng, Y.; Hu, X.; Xu, X.; Yang, X.; Song, Y.; Wang, R. Basal Plane Bending of 4H-SiC Single Crystals Grown by Sublimation Method with Different Seed Attachment Methods. *CrystEngComm* **2018**, *20*, 6957−6962.
(17) Imanishi, M.; Murakami, K.; Yamada, T.; Kakinouchi, K.; Nakamura, K.; Kitamura, T.; Okumura, K.; Yoshimura, M.; Mori, Y. Promotion of Lateral Growth of GaN Crystals on Point Seeds by Extraction of Substrates from Melt in the Na-Flux Method. *Appl. Phys. Express* **2019**, *12*, 045508.
(18) Grabianska, K.; Kucharski, R.; Puchalski, A.; Sochacki, T.; Bockowski, M. Recent Progress in Basic Ammonothermal GaN Crystal Growth. *J. Cryst. Growth* **2020**, *547*, 125804.
(19) Wei, T.-C.; Tsai, D.-S.; Ravadgar, P.; Ke, J.-J.; Tsai, M.-L.; Lien, D.-H.; Huang, C.-Y.; Horng, R.-H.; He, J.-H. See-Through Ga_2O_3 Solar-Blind Photodetectors for Use in Harsh Environments. *IEEE J. Sel. Top. Quantum Electron.* **2014**, *20*, 112−117.
(20) Orita, M.; Hiramatsu, H.; Ohta, H.; Hirano, M.; Hosono, H. Preparation of Highly Conductive, Deep Ultraviolet Transparent β-Ga_2O_3 Thin Film at Low Deposition Temperatures. *Thin Solid Films* **2002**, *411*, 134−139.
(21) Afzal, A. β-Ga_2O_3 Nanowires and Thin Films for Metal Oxide Semiconductor Gas Sensors: Sensing Mechanisms and Performance Enhancement Strategies. *J. Materiomics* **2019**, *5*, 542−557.
(22) Yu, Z.; Overgaard, C. D.; Droopad, R.; Passlack, M.; Abrokwah, J. K. Growth and Physical Properties of Ga_2O_3 Thin Films on GaAs(001) Substrate by Molecular-Beam Epitaxy. *Appl. Phys. Lett.* **2003**, *82*, 2978.
(23) Baliga, B. J. Semiconductors for High-Voltage, Vertical Channel Field-Effect Transistors. *J. Appl. Phys.* **1982**, *53*, 1759.
(24) Ahman, J.; Svensson, G.; Albertsson, J. A Reinvestigation of β-Gallium Oxide. *Acta Crystallogr., Sect. C: Cryst. Struct. Commun.* **1996**, *52*, 1336−1338.
(25) Yoshioka, S.; Hayashi, H.; Kuwabara, A.; Oba, F.; Matsunaga, K.; Tanaka, I. Structures and Energetics of Ga_2O_3 Polymorphs. *J. Phys.: Condens. Matter* **2007**, *19*, 346211.
(26) Hoshikawa, K.; Ohba, E.; Kobayashi, T.; Yanagisawa, J.; Miyagawa, C.; Nakamura, Y. Growth of β-Ga_2O_3 Single Crystals Using Vertical Bridgman Method in Ambient Air. *J. Cryst. Growth* **2016**, *447*, 36−41.
(27) Shinohara, D.; Fujita, S. Heteroepitaxy of Corundum-Structured α-Ga_2O_3 Thin Films on α-Al_2O_3 Substrates by Ultrasonic Mist Chemical Vapor Deposition. *Jpn. J. Appl. Phys.* **2008**, *47*, 7311−7313.
(28) Kan, S.-i.; Takemoto, S.; Kaneko, K.; Takahashi, I.; Sugimoto, M.; Shinohe, T.; Fujita, S. Electrical Properties of α-Ir_2O_3/α-Ga_2O_3 pn Heterojunction Diode and Band Alignment of the Heterostructure. *Appl. Phys. Lett.* **2018**, *113*, 212104.
(29) Oshima, Y.; Villora, E. G.; Matsushita, Y.; Yamamoto, S.; Shimamura, K. Epitaxial Growth of Phase-Pure ε-Ga_2O_3 by Halide Vapor Phase Epitaxy. *J. Appl. Phys.* **2015**, *118*, 085301.
(30) Mezzadri, F.; Calestani, G.; Boschi, F.; Delmonte, D.; Bosi, M.; Fornari, R. Crystal Structure and Ferroelectric Properties of ε-Ga_2O_3 Films Grown on (0001)-Sapphire. *Inorg. Chem.* **2016**, *55*, 12079−12084.
(31) Víllora, E. G.; Shimamura, K.; Ujiie, T.; Aoki, K. Electrical Conductivity and Lattice Expansion of β-Ga_2O_3 below Room Temperature. *Appl. Phys. Lett.* **2008**, *92*, 202118.
(32) Handwerg, M.; Mitdank, R.; Galazka, Z.; Fischer, S. F. Temperature-Dependent Thermal Conductivity in Mg-Doped and Undoped β-Ga_2O_3 Bulk-Crystals. *Semicond. Sci. Technol.* **2015**, *30*, 024006.
(33) Slomski, M.; Blumenschein, N.; Paskov, P. P.; Muth, J. F.; Paskova, T. Anisotropic Thermal Conductivity of β-Ga_2O_3 at Elevated Temperatures: Effect of Sn and Fe Dopants. *J. Appl. Phys.* **2017**, *121*, 235104.
(34) Fiedler, A.; Schewski, R.; Galazka, Z.; Irmscher, K. Static Dielectric Constant of β-Ga_2O_3 Perpendicular to the Principal Planes (100), (010), and (001). *ECS J. Solid State Sci. Technol.* **2019**, *8*, Q3083.

(35) Oshima, T.; Arai, N.; Suzuki, N.; Ohira, S.; Fujita, S. Surface Morphology of Homoepitaxial β-Ga_2O_3 Thin Films Grown by Molecular Beam Epitaxy. *Thin Solid Films* **2008**, *516*, 5768−5771.

(36) Tippins, H. H. Optical Absorption and Photoconductivity in the Band Edge of β-Ga_2O_3. *Phys. Rev.* **1965**, *140*, A316.

(37) Orita, M.; Ohta, H.; Hirano, M.; Hosono, H. Deep-Ultraviolet Transparent Conductive β-Ga_2O_3 Thin Films. *Appl. Phys. Lett.* **2000**, *77*, 4166.

(38) Higashiwaki, M.; Sasaki, K.; Kuramata, A.; Masui, T.; Yamakoshi, S. Development of Gallium Oxide Power Devices. *Phys. Status Solidi A* **2014**, *211*, 21−26.

(39) Sasaki, K.; Kuramata, A.; Masui, T.; Víllora, E. G.; Shimamura, K.; Yamakoshi, S. Device-Quality β-Ga_2O_3 Epitaxial Films Fabricated by Ozone Molecular Beam Epitaxy. *Appl. Phys. Express* **2012**, *5*, 035502.

(40) Peelaers, H.; Van de Walle, C. G. Brillouin Zone and Band Structure of β-Ga_2O_3. *Phys. Status Solidi B* **2015**, *252*, 828−832.

(41) Mohamed, M.; Janowitz, C.; Unger, I.; Manzke, R.; Galazka, Z.; Uecker, R.; Fornari, R.; Weber, J. R.; Varley, J. B.; Walle, C. G. V. d. The Electronic Structure of β-Ga_2O_3. *Appl. Phys. Lett.* **2010**, *97*, 211903.

(42) Chase, A. B. Growth of β-Ga_2O_3 by the Verneuil Technique. *J. Am. Ceram. Soc.* **1964**, *47*, 470.

(43) Vasyltsiv, V. I.; Rym, Y. I.; Zakharko, Y. Optical Absorption and Photoconductivity at the Band Edge of β-$Ga_{2-x}In_xO_3$. *Phys. Status Solidi B* **1996**, *195*, 653−658.

(44) Tomm, Y.; Ko, J. M.; Yoshikawa, A.; Fukuda, T. Floating Zone Growth of β-Ga_2O_3: a New Window Material for Optoelectronic Device Applications. *Sol. Energy Mater. Sol. Cells* **2001**, *66*, 369−374.

(45) Villora, E. G.; Shimamura, K.; Yoshikawa, Y.; Aoki, K.; Ichinose, N. Large-Size β-Ga_2O_3 Single Crystals and Wafers. *J. Cryst. Growth* **2004**, *270*, 420−426.

(46) Zhang, J.; Li, B.; Xia, C.; Pei, G.; Deng, Q.; Yang, Z.; Xu, W.; Shi, H.; Wu, F.; Wu, Y.; Xu, J. Growth and Spectral Characterization of β-Ga_2O_3 Single crystals. *J. Phys. Chem. Solids* **2006**, *67*, 2448−2451.

(47) Suzuki, N.; Ohira, S.; Tanaka, M.; Sugawara, T.; Nakajima, K.; Shishido, T. Fabrication and Characterization of Transparent Conductive Sn-doped β-Ga_2O_3 Single Crystal. *Phys. Status Solidi C* **2007**, *4*, 2310−2313.

(48) Fujita, Y.; Nagao, M.; Maruyama, Y.; Watauchi, S.; Miki, K.; Tanaka, I. Solubility of Iridium into β-Ga_2O_3 Single Crystals Grown by Floating Zone Method. *J. Cryst. Growth* **2022**, *584*, 126581.

(49) Galazka, Z.; Uecker, R.; Irmscher, K.; Albrecht, M.; Klimm, D.; Pietsch, M.; Brützam, M.; Bertram, R.; Ganschow, S.; Fornari, R. Czochralski Growth and Characterization of β-Ga_2O_3 Single Crystals. *Cryst. Res. Technol.* **2010**, *45*, 1229−1236.

(50) Irmscher, K.; Galazka, Z.; Pietsch, M.; Uecker, R.; Fornari, R. Electrical Properties of β-Ga_2O_3 Single Crystals Grown by the Czochralski Method. *J. Appl. Phys.* **2011**, *110*, 063720.

(51) Galazka, Z.; Irmscher, K.; Uecker, R.; Bertram, R.; Pietsch, M.; Kwasniewski, A.; Naumann, M.; Schulz, T.; Schewski, R.; Klimm, D.; Bickermann, M. On the Bulk β-Ga_2O_3 Single Crystals Grown by the Czochralski Method. *J. Cryst. Growth* **2014**, *404*, 184−191.

(52) Galazka, Z.; Uecker, R.; Klimm, D.; Irmscher, K.; Naumann, M.; Pietsch, M.; Kwasniewski, A.; Bertram, R.; Ganschow, S.; Bickermann, M. Scaling-Up of Bulk β-Ga_2O_3 Single Crystals by the Czochralski Method. *ECS J. Solid State Sci. Technol.* **2017**, *6*, Q3007−Q3011.

(53) Blevins, J. D.; Stevens, K.; Foundos, G.; Lindsey, A.; Sande, L. Development of Large Diameter Semi-Insulating Gallium Oxide (Ga_2O_3) Substrates. *IEEE Trans. Semicond. Manuf.* **2019**, *32*, 466−472.

(54) Galazka, Z.; Irmscher, K.; Schewski, R.; Hanke, I. M.; Pietsch, M.; Ganschow, S.; Klimm, D.; Dittmar, A.; Fiedler, A.; Schroeder, T.; Bickermann, M. *J. Cryst. Growth* **2020**, *529*, 125297.

(55) Bauman, D. A.; Panov, D. I.; Zakgeim, D. A.; Spiridonov, V. A.; Kremleva, A. V.; Petrenko, A. A.; Brunkov, P. N.; Prasolov, N. D.; Nashchekin, A. V.; Smirnov, A. M.; Odnoblyudov, M. A.; Bougrov, V. E.; Romanov, A. E. High-Quality Bulk β-Ga_2O_3 and β-$(Al_xGa_{1-x})_2O_3$ Crystals: Growth and Properties. *Phys. Status Solidi A* **2021**, *218*, 2100335.

(56) Galazka, Z. Growth of Bulk β-Ga_2O_3 Single Crystals by the Czochralski Method. *J. Appl. Phys.* **2022**, *131*, 031103.

(57) Kuramata, A.; Koshi, K.; Watanabe, S.; Yamaoka, Y.; Masui, T.; Yamakoshi, S. High-Quality β-Ga_2O_3 Single Crystals Grown by Edge-Defined Film-Fed Growth. *J. Jpn. Appl. Phys.* **2016**, *55*, 1202A2.

(58) Fu, B.; Mu, W.; Zhang, J.; Wang, X.; Zhuang, W.; Yin, Y.; Jia, Z.; Tao, X. A Study on the Technical Improvement and the Crystalline Quality Optimization of Columnar β-Ga_2O_3 Crystal Growth by an EFG Method. *CrystEngComm* **2020**, *22*, 5060−5066.

(59) Mohamed, H. F.; Xia, C.; Sai, Q.; Cui, H.; Pan, M.; Qi, H. Growth and Fundamentals of bulk β-Ga_2O_3 Single Crystals. *J. Semicond.* **2019**, *40*, 011801.

(60) Galazka, Z. *Czochralski Method.* In Gallium Oxide, Higashiwaki, M.; Fujita, S., Eds.; Springer Series in Materials Science; Springer: Cham, 2020; Vol *293*.

(61) Baldini, M.; Albrecht, M.; Fiedler, A.; Irmscher, K.; Klimm, D.; Schewski, R.; Wagner, G. Semiconducting Sn-doped β-Ga_2O_3 Homoepitaxial Layers Grown by Metal Organic Vapour-Phase Epitaxy. *J. Mater. Sci.* **2016**, *51*, 3650−3656.

(62) Schewski, R.; Baldini, M.; Irmscher, K.; Fiedler, A.; Markurt, T.; Neuschulz, B.; Remmele, T.; Schulz, T.; Wagner, G.; Galazka, Z.; Albrecht, M. Evolution of Planar Defects during Homoepitaxial Growth of β-Ga2O3 Layers on (100) Substrates-a Quantitative Model. *J. Appl. Phys.* **2016**, *120*, 225308.

(63) Fiedler, A.; Schewski, R.; Baldini, M.; Galazka, Z.; Wagner, G.; Albrecht, M.; Irmscher, K. Influence of Incoherent Twin Boundaries on the Electrical Properties of β-Ga_2O_3 Layers Homoepitaxially Grown by Metal-Organic Vapor Phase Epitaxy. *J. Appl. Phys.* **2017**, *122*, 165701.

(64) Baldini, M.; Albrecht, M.; Fiedler, A.; Irmscher, K.; Schewski, R.; Wagner, G. Editors' Choice-Si- and Sn-Doped Homoepitaxial β-Ga_2O_3 Layers Grown by MOVPE on (010)-Oriented Substrates. *ECS J. Solid State Sci. Technol.* **2017**, *6*, Q3040−Q3044.

(65) Rafique, S.; Han, L.; Tadjer, M. J.; Freitas, J. A.; Mahadik, N. A.; Zhao, H. Homoepitaxial Growth of β-Ga_2O_3 Thin Films by Low Pressure Chemical Vapor Deposition. *Appl. Phys. Lett.* **2016**, *108*, 182105.

(66) Murakami, H.; Nomura, K.; Goto, K.; Sasaki, K.; Kawara, K.; Thieu, Q. T.; Togashi, R.; Kumagai, Y.; Higashiwaki, M.; Kuramata, A.; Yamakoshi, S.; Monemar, B.; Koukitu, A. *Appl. Phys. Express* **2015**, *8*, 015503.

(67) Tadjer, M. J.; Mastro, M. A.; Mahadik, N. A.; Currie, M.; Wheeler, V. D.; Freitas Jr, J. A.; Greenlee, J. D.; Hite, J. K.; Hobart, K. D.; Eddy Jr, C. R.; Kub, F. J. Structural, Optical, and Electrical Characterization of Monoclinic β-Ga_2O_3 Grown by MOVPE on Sapphire Substrates. *J. Electron. Mater.* **2016**, *45*, 2031−2037.

(68) Gogova, D.; Schmidbauer, M.; Kwasniewski, A. Homo- and Heteroepitaxial Growth of Sn-Doped β-Ga_2O_3 Layers by MOVPE. *CrystEngComm* **2015**, *17*, 6744−6752.

(69) Schewski, R.; Wagner, G.; Baldini, M.; Gogova, D.; Galazka, Z.; Schulz, T.; Remmele, T.; Markurt, T.; von Wenckstern, H.; Grundmann, M.; Bierwagen, O.; Vogt, P.; Albrecht, M. Epitaxial Stabilization of Pseudomorphic α-Ga_2O_3 on sapphire (0001). *Appl. Phys. Express* **2015**, *8*, 011101.

(70) Chen, Y.; Liang, H.; Xia, X.; Tao, P.; Shen, R.; Liu, Y.; Feng, Y.; Zheng, Y.; Li, X.; Du, G. The Lattice Distortion of β-Ga_2O_3 Film Grown on *c*-plane Sapphire. *J. Mater. Sci.: Mater. Electron.* **2015**, *26*, 3231−3235.

(71) Yoshioka, S.; Hayashi, H.; Kuwabara, A.; Oba, F.; Matsunaga, K.; Tanaka, I. Structures and Energetics of Ga_2O_3 polymorphs. *J. Phys.: Condens. Matter* **2007**, *19*, 346211.

(72) Boschi, F.; Bosi, M.; Berzina, T.; Buffagni, E.; Ferrari, C.; Fornari, R. Hetero-Epitaxy of ε-Ga_2O_3 Layers by MOCVD and ALD. *J. Cryst. Growth* **2016**, *443*, 25−30.

(73) Cora, I.; Mezzadri, F.; Boschi, F.; Bosi, M.; Čaplovičová, M.; Calestani, G.; Dódony, I.; Pécza, B.; Fornaric, R. The real structure of

ε-Ga_2O_3 and its relation to κ-phase. *CrystEngComm* **2017**, *19*, 1509−1516.
(74) Pavesi, M.; Fabbri, F.; Boschi, F.; Piacentini, G.; Baraldi, A.; Bosi, M.; Gombia, E.; Parisini, A.; Fornari, R. ε-Ga_2O_3 Epilayers as a Material for Solar-Blind UV Photodetectors. *Mater. Chem. Phys.* **2018**, *205*, 502−507.
(75) Fornari, R.; Pavesi, M.; Montedoro, V.; Klimm, D.; Mezzadri, F.; Cora, I.; Pecz, B.; Boschi, F.; Parisini, A.; Baraldi, A.; Ferrari, C.; Gombia, E.; Bosi, M. Thermal Stability of ε-Ga_2O_3 Polymorph. *Acta Mater.* **2017**, *140*, 411−416.
(76) Zhuo, Y.; Chen, Z.; Tu, W.; Ma, X.; Pei, Y.; Wang, G. β-Ga_2O_3 versus ε-Ga_2O_3: Control of the Crystal Phase Composition of Gallium Oxide Thin Film Prepared by Metal-Organic Chemical Vapor Deposition. *Appl. Surf. Sci.* **2017**, *420*, 802−807.
(77) Xia, X.; Chen, Y.; Feng, Q.; Liang, H.; Tao, P.; Xu, M.; Du, G. Hexagonal Phase-Pure Wide Band Gap ε-Ga_2O_3 Films Grown on 6H-SiC Substrates by Metal Organic Chemical Vapor Deposition. *Appl. Phys. Lett.* **2016**, *108*, 202103.
(78) Tsai, M.-Y.; Bierwagen, O.; White, M. E.; Speck, J. S. β-Ga_2O_3 Growth by Plasma-Assisted Molecular Beam Epitaxy. *J. Vac. Sci. Technol. A* **2010**, *28*, 354.
(79) Oshima, Y.; Ahmadi, E.; Kaun, S.; Wu, F.; Speck, J. S. Growth and Etching Characteristics of (001) β-Ga_2O_3 by Plasma-Assisted Molecular Beam Epitaxy. *Semicond. Sci. Technol.* **2018**, *33*, 015013.
(80) Nakagomi, S.; Kokubun, Y. Crystal Orientation of β-Ga_2O_3 Thin Films Formed on *c*-plane and *a*-plane Sapphire Substrate. *J. Cryst. Growth* **2012**, *349*, 12−18.
(81) Oshima, Y.; Víllora, E. G.; Shimamura, K. Quasi-Heteroepitaxial Growth of β-Ga_2O_3 on Off-Angled Sapphire (0 0 0 1) Substrates by Halide Vapor Phase Epitaxy. *J. Cryst. Growth* **2015**, *410*, 53−58.
(82) Lee, S.-D.; Akaiwa, K.; Fujita, S. Thermal Stability of Single Crystalline Alpha Gallium Oxide Films on Sapphire Substrates. *Phys. Status Solidi C* **2013**, *10*, 1592−1595.
(83) Baliga, B. J. Power Semiconductor Device Figure of Merit for High-Frequency Applications. *IEEE Electron Device Lett.* **1989**, *10*, 455−457.
(84) Wong, M. H.; Sasaki, K.; Kuramata, A.; Yamakoshi, S.; Higashiwaki, M. Field-Plated Ga_2O_3 MOSFETs with a Breakdown Voltage of Over 750 V. *IEEE Electron Device Lett.* **2016**, *37*, 212−215.
(85) Higashiwaki, M.; Sasaki, K.; Kamimura, T.; Wong, M. H.; Krishnamurthy, D.; Kuramata, A.; Masui, T.; Yamakoshi, S. Depletion-Mode Ga_2O_3 Metal-Oxide-Semiconductor Field-Effect Transistors on β-Ga_2O_3 (010) Substrates and Temperature Dependence of Their Device Characteristics. *Appl. Phys. Lett.* **2013**, *103*, 123511.
(86) Wong, M. H.; Sasaki, K.; Kuramata, A.; Yamakoshi, S.; Higashiwaki, M. Electron Channel Mobility in Silicon-Doped Ga_2O_3 MOSFETs with a Resistive Buffer Layer. *Jpn. J. Appl. Phys.* **2016**, *55*, 1202B9.
(87) Moser, N.; McCandless, J.; Crespo, A.; Leedy, K.; Green, A.; Neal, A.; Mou, S.; Ahmadi, E.; Speck, J.; Chabak, K.; Peixoto, N.; Jessen, G. Ge-Doped β-Ga_2O_3 MOSFETs. *IEEE Electron Device Lett.* **2017**, *38*, 775−778.
(88) Green, A. J.; Chabak, K. D.; Heller, E. R.; Fitch, R. C., Jr.; Baldini, M.; Fiedler, A.; Irmscher, K.; Wagner, G.; Galazka, Z.; Tetlak, S. E.; Crespo, A.; Leedy, K.; Jessen, G. H. 3.8-MV/cm Breakdown Strength of MOVPE-Grown Sn-Doped β-Ga_2O_3 MOSFETs. *IEEE Electron Device Lett.* **2016**, *37*, 902−905.
(89) Zeng, K.; Vaidya, A.; Singisetti, U. 1.85 kV Breakdown Voltage in Lateral Field-Plated Ga2O3MOSFETs. *IEEE Electron Device Lett.* **2018**, *39*, 1385−1388.
(90) Tipirneni, N.; Koudymov, A.; Adivarahan, V.; Yang, J.; Simin, G.; Khan, M. A. The 1.6-kV AlGaN/GaN HFETs. *IEEE Electron Device Lett.* **2006**, *27*, 716−718.
(91) Dora, Y.; Chakraborty, A.; McCarthy, L.; Keller, S.; DenBaars, S. P.; Mishra, U. K. High Breakdown Voltage Achieved on AlGaN/GaN HEMTs with Integrated Slant Field Plates. *IEEE Electron Device Lett.* **2006**, *27*, 713−715.
(92) Lv, Y.; Zhou, X.; Long, S.; Song, X.; Wang, Y.; Liang, S.; He, Z.; Han, T.; Tan, X.; Feng, Z.; Dong, H.; Zhou, X.; Yu, Y.; Cai, S.; Liu, M. Source-Field-Plated β-Ga_2O_3 MOSFET with Record Power Figure of Merit of 50.4 MW/cm^2. *IEEE Electron Device Lett.* **2019**, *40*, 83−86.
(93) Mun, J. K.; Cho, K.; Chang, W.; Jung, H.-W.; Do, J. 2.32 kV Breakdown Voltage Lateral β-Ga_2O_3 MOSFETs with Source-Connected Field Plate. *ECS J. Solid State Sci. Technol.* **2019**, *8*, Q3079−Q3082.
(94) Tetzner, K.; Treidel, E. B.; Hilt, O.; Popp, A.; Anooz, S. B.; Wagner, G.; Thies, A.; Ickert, K.; Gargouri, H.; Würfl, J. Lateral 1.8 kV β-Ga_2O_3 MOSFET with 155 MW/cm^2 Power Figure of Merit. *IEEE Electron Device Lett.* **2019**, *40*, 1503−1506.
(95) Krishnamoorthy, S.; Xia, Z.; Joishi, C.; Zhang, Y.; McGlone, J.; Johnson, J.; Brenner, M.; Arehart, A. R.; Hwang, J.; Lodha, S.; Rajan, S. Modulation-Doped β-$(Al_{0.2}Ga_{0.8})_2O_3/Ga_2O_3$ Field-Effect Transistor. *Appl. Phys. Lett.* **2017**, *111*, 023502.
(96) Zhang, Y.; Neal, A.; Xia, Z.; Joishi, C.; Johnson, J. M.; Zheng, Y.; Bajaj, S.; Brenner, M.; Dorsey, D.; Chabak, K.; Jessen, G.; Hwang, J.; Mou, S.; Heremans, J. P.; Rajan, S. Demonstration of High Mobility and Quantum Transport in Modulation-Doped β-$(Al_xGa_{1-x})_2O_3/Ga_2O_3$ Heterostructures. *Appl. Phys. Lett.* **2018**, *112*, 173502.
(97) Joishi, C.; Zhang, Y.; Xia, Z.; Sun, W.; Arehart, A. R.; Ringel, S.; Lodha, S.; Rajan, S. Breakdown Characteristics of β-$(Al_{0.22}Ga_{0.78})_2O_3/Ga_2O_3$ Field-Plated Modulation-Doped Field-Effect Transistors. *IEEE Electron Device Lett.* **2019**, *40*, 1241−1244.
(98) Ahmadi, E.; Koksaldi, O. S.; Zheng, X.; Mates, T.; Oshima, Y.; Mishra, U. K.; Speck, J. S. Demonstration of β-$(Al_xGa_{1-x})_2O_3/\beta$-$Ga_2O_3$ Modulation Doped Field-Effect Transistors with Ge as Dopant Grown via Plasma-Assisted Molecular Beam Epitaxy. *Appl. Phys. Express* **2017**, *10*, 071101.
(99) Lei, Y.; Shi, H.; Lu, H.; Chen, D.; Zhang, R.; Zheng, Y. Field Plate Engineering for GaN-based Schottky Barrier Diodes. *J. Semicond.* **2013**, *34*, 054007.
(100) Lipkin, L. A.; Palmour, J. W. Insulator Investigation on SiC for Improved Reliability. *IEEE Trans. Electron Devices* **1999**, *46*, 525−532.
(101) Lee, M.-H.; Peterson, R. Interfacial Reactions of Titanium/Gold Ohmic Contacts with Sn-Doped β-Ga_2O_3. *APL Mater.* **2019**, *7*, 022524.
(102) Sasaki, K.; Higashiwaki, M.; Kuramata, A.; Masui, T.; Yamakoshi, S. Si-Ion Implantation Doping in β-Ga_2O_3 and Its Application to Fabrication of Low-Resistance Ohmic Contacts. *Appl. Phys. Express* **2013**, *6*, 086502.
(103) Zeng, K.; Wallace, J. S.; Heimburger, C.; Sasaki, K.; Kuramata, A.; Masui, T.; Gardella, J. A., Jr.; Singisetti, U. Ga_2O_3 MOSFETs Using Spin-On-Glass Source/Drain Doping Technology. *IEEE Electron Device Lett.* **2017**, *38*, 513−516.
(104) Jeong, Y. J.; Yang, J. Y.; Lee, C. H.; Park, R.; Lee, G.; Chung, R. B. K.; Yoo, G. Fluorine-Based Plasma Treatment for Hetero-Epitaxial β-Ga_2O_3 MOSFETs. *Appl. Surf. Sci.* **2021**, *558*, 149936.
(105) Ghosh, K.; Singisetti, U. Ab Initio Velocity-Field Curves in Monoclinic β-Ga_2O_3. *J. Appl. Phys.* **2017**, *122*, 035702.
(106) Green, A. J.; Chabak, K. D.; Baldini, M.; Moser, N.; Gilbert, R.; Fitch, R. C., Jr.; Wagner, G.; Galazka, Z.; McCandless, J.; Crespo, A.; Leedy, K.; Jessen, G. H. β-Ga_2O_3 MOSFETs for Radio Frequency Operation. *IEEE Electron Device Lett.* **2017**, *38*, 790−793.
(107) Liddy, K. J.; Green, A. J.; Hendricks, N. S.; Heller, E. R.; Moser, N. A.; Leedy, K. D.; Popp, A.; Lindquist, M. T.; Tetlak, S. E.; Wagner, G.; Chabak, K. D.; Jessen, G. H. Thin Channel β-Ga_2O_3 MOSFETs with Self-Aligned Refractory Metal Gates. *Appl. Phys. Express* **2019**, *12*, 126501.
(108) Xia, Z.; Xue, H.; Joishi, C.; McGlone, J.; Kalarickal, N. K.; Sohel, S. H.; Brenner, M. B.; Arehart, A.; Ringel, S.; Lodha, S.; Lu, W.; Rajan, S. β-Ga_2O_3 Delta-Doped Field-Effect Transistors with Current Gain Cutoff Frequency of 27 GHz. *IEEE Electron Device Lett.* **2019**, *40*, 1052−1055.
(109) Lv, Y.; Liu, H.; Wang, Y.; Fu, X.; Ma, C.; Song, X.; Zhou, X.; Zhang, Y.; Dong, P.; Du, H.; Liang, S.; Han, T.; Zhang, J.; Feng, Z.;

Zhou, H.; Cai, S.; Hao, Y. Oxygen Annealing Impact on β-Ga_2O_3 MOSFETs: Improved Pinch-Off Characteristic and Output Power Density. *Appl. Phys. Lett.* **2020**, *117*, 133503.

(110) Im, K.-S.; Won, C.-H.; Jo, Y.-W.; Lee, J.-H.; Bawedin, M.; Cristoloveanu, S.; Lee, J.-H. High-Performance GaN-Based Nano-channel FinFETs With/Without AlGaN/GaN Heterostructure. *IEEE Trans. Electron Devices* **2013**, *60*, 3012−3018.

(111) Im, K.-S.; Sindhuri, V.; Jo, Y.-W.; Son, D.-H.; Lee, J.-H.; Cristoloveanu, S.; Lee, J.-H. Fabrication of AlGaN/GaN Ω-Shaped Nanowire Fin-Shaped FETs by a Top-Down Approach. *Appl. Phys. Express* **2015**, *8*, 066501.

(112) Chabak, K. D.; Moser, N.; Green, A. J.; Walker, D. E., Jr.; Tetlak, S. E.; Heller, E.; Crespo, A.; Fitch, R.; McCandless, J. P.; Leedy, K.; Baldini, M.; Wagner, G.; Galazka, Z.; Li, X.; Jessen, G. Enhancement-Mode Ga_2O_3 Wrap-Gate Fin Field-Effect Transistors on Native (100) β-Ga_2O_3 Substrate with High Breakdown Voltage. *Appl. Phys. Lett.* **2016**, *109*, 213501.

(113) Wong, M. H.; Nakata, Y.; Kuramata, A.; Yamakoshi, S.; Higashiwaki, M. Enhancement-Mode Ga_2O_3 MOSFETs with Si-Ion-Implanted Source and Drain. *Appl. Phys. Express* **2017**, *10*, 041101.

(114) Lv, Y.; Zhou, X.; Long, S.; Wang, Y.; Song, X.; Zhou, X.; Xu, G.; Liang, S.; Feng, Z.; Cai, S.; Fu, X.; Pu, A.; Liu, M. Enhancement-Mode β-Ga_2O_3 Metal-Oxide-Semiconductor Field-Effect Transistor with High Breakdown Voltage over 3000 V Realized by Oxygen Annealing. *Phys. Status Solidi RRL* **2020**, *14*, 1900586.

(115) Chabak, K. D.; McCandless, J. P.; Moser, N. A.; Green, A. J.; Mahalingam, K.; Crespo, A.; Hendricks, N.; Howe, B. M.; Tetlak, S. E.; Leedy, K.; Fitch, R. C.; Wakimoto, D.; Sasaki, K.; Kuramata, A.; Jessen, G. H. Recessed-Gate Enhancement-Mode β-Ga_2O_3 MOS-FETs. *IEEE Electron Device Lett.* **2018**, *39*, 67−70.

(116) Yoon, Y.; Kim, M. J.; Cho, B. J.; Shin, M.; Hwang, W. S. An 8-nm-Thick Sn-Doped Polycrystalline β-Ga_2O_3 MOSFET with a "Normally Off" Operation. *Appl. Phys. Lett.* **2021**, *119*, 122103.

(117) Hu, Z.; Nomoto, K.; Li, W.; Tanen, N.; Sasaki, K.; Kuramata, A.; Nakamura, T.; Jena, D.; Xing, H. G. Enhancement-Mode Ga_2O_3 Vertical Transistors with Breakdown Voltage > 1 kV. *IEEE Electron Device Lett.* **2018**, *39*, 869−872.

(118) Wong, M. H.; Murakami, H.; Kumagai, Y.; Higashiwaki, M. Enhancement-Mode β-Ga_2O_3 Current Aperture Vertical MOSFETs with N-Ion-Implanted Blocker. *IEEE Electron Device Lett.* **2020**, *41*, 296−299.

(119) Dong, L.; Jia, R.; Li, C.; Xin, B.; Zhang, Y. Ab Initio Study of N-Doped β-Ga_2O_3 with Intrinsic Defects: The Structural, Electronic and Optical Properties. *J. Alloys Compd.* **2017**, *712*, 379−385.

(120) Lyons, J. L. A Survey of Acceptor Dopants for β-Ga_2O_3. *Semicond. Sci. Technol.* **2018**, *33*, 05LT02.

(121) Peelaers, H.; Lyons, J. L.; Varley, J. B.; Van de Walle, C. G. Deep Acceptors and Their Diffusion in Ga_2O_3. *APL Mater.* **2019**, *7*, 022519.

(122) Kamimura, T.; Nakata, Y.; Wong, M. H.; Higashiwaki, M. Normally-Off Ga_2O_3 MOSFETs with Unintentionally Nitrogen-Doped Channel Layer Grown by Plasma-Assisted Molecular Beam Epitaxy. *IEEE Electron Device Lett.* **2019**, *40*, 1064−1067.

(123) Hwang, W. S.; Verma, A.; Peelaers, H.; Protasenko, V.; Rouvimov, S.; Xing, H.; Seabaugh, A.; Haensch, W.; Walle, C. V. d.; Galazka, Z.; Albrecht, M.; Fornari, R.; Jena, D. High-Voltage Field Effect Transistors with Wide-Bandgap β-Ga_2O_3 Nanomembranes. *Appl. Phys. Lett.* **2014**, *104*, 203111.

(124) Novoselov, K. S.; Geim, A. K.; Morozov, S. V.; Jiang, D.; Zhang, Y.; Dubonos, S. V.; Grigorieva, I. V.; Firsov, A. A. Electric Field Effect in Atomically Thin Carbon Films. *Science* **2004**, *306*, 666−669.

(125) Radisavljevic, B.; Radenovic, A.; Brivio, J.; Giacometti, V.; Kis, A. Single-Layer MoS_2 Transistors. *Nat. Nanotechnol.* **2011**, *6*, 147−150.

(126) Fang, H.; Chuang, S.; Chang, T. C.; Takei, K.; Takahashi, T.; Javey, A. High-Performance Single Layered WSe_2 p-FETs with Chemically Doped Contacts. *Nano Lett.* **2012**, *12*, 3788−3792.

(127) Zhou, H.; Si, M.; Alghamdi, S.; Qiu, G.; Yang, L.; Ye, P. D. High-Performance Depletion/Enhancement Mode β-Ga_2O_3 on Insulator (GOOI) Field-Effect Transistors with Record Drain Currents of 600/450 mA/mm. *IEEE Electron Device Lett.* **2017**, *38*, 103−106.

(128) Kim, J.; Tadjer, M. J.; Mastro, M. A.; Kim, J. Controlling the Threshold Voltage of β-Ga_2O_3 Field-Effect Transistors via Remote Fluorine Plasma Treatment. *J. Mater. Chem. C* **2019**, *7*, 8855−8860.

(129) Wang, X.; Yan, S.; Mu, W.; Jia, Z.; Zhang, J.; Xin, Q.; Tao, X.; Song, A. Enhancement-Mode Ga_2O_3 FET with High Mobility Using p-Type SnO Heterojunction. *IEEE Electron Device Lett.* **2022**, *43*, 44−47.

(130) Kim, J.; Oh, S.; Mastro, M. A.; Kim, J. Exfoliated β-Ga_2O_3 Nano-Belt Field-Effect Transistors for Air-Stable High Power and High Temperature Electronics. *Phys. Chem. Chem. Phys.* **2016**, *18*, 15760−15764.

(131) Ma, J.; Lee, O.; Yoo, G. Effect of Al_2O_3 Passivation on Electrical Properties of β-Ga_2O_3 Field-Effect Transistor. *IEEE J. Electron Devices Soc.* **2019**, *7*, 512−516.

(132) Ma, J.; Cho, H. J.; Heo, J.; Kim, S.; Yoo, G. Asymmetric Double-Gate β-Ga_2O_3 Nanomembrane Field-Effect Transistor for Energy-Efficient Power Devices. *Adv. Electron. Mater.* **2019**, *5*, 1800938.

(133) Kim, J.; Kim, J. Monolithically Integrated Enhancement-Mode and Depletion-Mode β-Ga2O3MESFETs with Graphene-Gate Architectures and Their Logic Applications. *ACS Appl. Mater. Interfaces* **2020**, *12*, 7310−7316.

(134) Kim, K.-T.; Jin, H.-J.; Choi, W.; Jeong, Y.; Shin, H. G.; Lee, Y.; Kim, K.; Im, S. High Performance β-Ga_2O_3 Schottky Barrier Transistors with Large Work Function TMD Gate of NbS_2 and TaS_2. *Adv. Funct. Mater.* **2021**, *31*, 2010303.

(135) Kim, J.; Mastro, M. A.; Tadjer, M. J.; Kim, J. Heterostructure WSe_2-Ga_2O_3 Junction Field-Effect Transistor for Low-Dimensional High-Power Electronics. *ACS Appl. Mater. Interfaces* **2018**, *10*, 29724−29729.

(136) Li, C.; Chen, C.; Chen, J.; He, T.; Li, H.; Yang, Z.; Xie, L.; Wang, Z.; Zhang, K. High-Performance Junction Field-Effect Transistor Based on Black Phosphorus/β-Ga_2O_3 Heterostructure. *J. Semicond.* **2020**, *41*, 082002.

(137) Lee, D.; Kim, H. W.; Kim, J.; Moon, J. H.; Lee, G.; Kim, J. Ultra-Wide Bandgap β-Ga_2O_3 Heterojunction Field-Effect Transistor Using p-Type 4H-SiC Gate for Efficient Thermal Management. *ECS J. Solid State Sci. Technol.* **2020**, *9*, 065006.

(138) Choi, W.; Ahn, J.; Kim, K.-T.; Jin, H.-J.; Hong, S.; Hwang, D. K.; Im, S. Ambipolar Channel p-TMD/n-Ga_2O_3 Junction Field Effect Transistors and High Speed Photo-sensing in TMD Channel. *Adv. Mater.* **2021**, *33*, 2103079.

https://doi.org/10.1021/acsomega.2c03345
ACS Omega 2022, 7, 36070−36091